Rip off and characterization of nanowire ensembles for photovoltaic applications

Master of Science Thesis

Seyed Alireza Abrand Abadizadeh

Supervisors:

Magnus Borgström

Damir Asoli

LUND UNIVERSITY

Division of Solid State Physics
Department of Physics

December 2013

Acknowledgement:

My deepest appreciation and thanks to my supervisor *Magnus Borgström*, for providing me the opportunity of experiencing a research in Nanoscience field and for his support and guidance throughout my master's project. I am also deeply indebted to my co-supervisor *Damir Asoli* for his full-time contribution, guidance, training and most importantly, his friendship; without his training I would not have managed much.

I would also like to show my gratitude to all the SolVoltaic AB Company staff members, especially *Ingvar Åberg* for his valuable advice during the meetings and *Andreas Dahlgren* for all the great time we have had in the Lab. I would also like to thank *Prof. Lars Samuelson* for introducing me to SolVoltaic AB Company.

Last but not least my family for their encouragement, inspiration and love. Without the support of my parents I could not complete my study. Thank you with all my love.

Abstract

The main aim of this project was to peel off the epitaxially grown nanowires (NWs) from their native substrate and transfer them to the cheaper carrier substrate in order to make solar cell device from transferred NWs. Potentially the peeling and transferring idea is about to decrease the cost of NWs growth by reusing the native substrate especially for expensive material such as InP and GaAs which are suitable materials for single junction solar cell. Two different kinds of polymers, PDMS and a SolOne^{TM} were used in this work as a membrane to peel off the NWs. Successful peeling was achieved which provides an opportunity to make photoluminescence and absorption measurements on ordered arrays of NWs embedded into membrane.

Transmission and reflection measurements were done on NWs embedded in membrane, after peeling, in order to experimentally measure the absorption through the ordered array of NWs without any contribution of the substrate. To fabricate a solar cell device from peeled off NWs, an ordered array of NWs with 2500 nm in length and 180 nm diameter with 400 nm of pitch was used. After peeling, the back contact was applied to the back of the membrane by metal deposition, and the membrane was bonded to the carrier substrate (silicon wafer was used in this projects) from the backside. After planarization, two different sizes of top contact were defined by photoresist spinning and lithography. Indium tin oxide (ITO), which is the transparent conductive oxide, was deposited on the top of the NWs as top contact.

I-V measurements under dark and illumination, which was provided by solar simulator, were performed to observe the fabricated device performance.

Table of Contents

1. Introduction

Nanotechnology has received huge attention recently by exhibiting novel properties and capability of manipulating the materials in order to tailor their properties for broad range of applications in different fields of science such as organic chemistry, molecular biology and semiconductor physics. This new field of science still needs much more research and work on the synthesis of nanomaterials, new characterization methods and tools and device fabrication techniques to improve knowledge of nanosystems and development mechanisms before getting into industrial manufacturing [1][2].

The main aim of this project was investigation and developments of techniques to peel off nanowire arrays from native substrates, which act as a carrier substrate after growth, and transfer them to another cheap carrier substrate such as silicon (Si) or glass. NWs should be processed vertically, and include contact formation for solar cell fabrication. This work is including optical and electrical characterization of peeled off NWs by conventional techniques such as spectroscopy, photoluminescence and current-voltage measurement to evaluate the physical properties of the device and also the capability of this peel off method. This idea helps to reduce the production cost of nanowire solar cells or any other devices defined by NW arrays, for instance nanowire LEDs, by reusing the native substrate after peeling and also some more application by making devices flexible.

Nanowires are a new class of materials, where the wire is in nano scale with diameter variation from tens of nanometers to hundreds of nanometers and length from few micrometer to hundreds of micrometer. The geometric design and properties of the nanowire make it a really good candidate for novel electronic and optoelectronic devices [3][4]. A broad range of material compositions can be grown heteroepitaxially in NW form due to efficient strain relaxation via the free surface [5], which is not possible for bulk and thin-film geometry. There are two main different approaches of nanowire synthesis; top-down approach where the bulk substrate will be selectively etched down to form the nanowires, and the bottom-up approach where nanowires will be formed by epitaxial growth, layer by layer, on the substrate [6][7][8].

2. Background

2.1 Solar Power, the only long-term solution

On the one hand, increasing consumption of electrical power, and on the other hand diminishing of the fossil fuel supply (which is the main source of energy to produce electricity in generators) have enforced human civilization to find good alternative sources to produce electricity that can also provide their increasing power demand in next few decades. During the last century the consumption of finite reserves fossil fuel greatly increased, just Oil consumption increased from 1.53 Gt in 1965 to 3.93 Gt in 2008 [9]. According to Central Intelligence Agency all already known oil reserves will be run out by 2052 if current rate of oil consumption goes on without considering population and consumption growth [9]. Even by considering coal and gas deposits we can carry on until 2088. Figure 2.1(a) shows the amount of already known oil, coal and gas reserves versus years; these reserves will be run out earlier since rate of power consumption is not standing still.
Global Warming is the other huge issue that the human civilization faces, and greenhouse gases are the main cause of that; Carbon dioxide (CO_2) is one of these gases that is mainly produced by burning fossil fuel. Burning that huge amount of fossil fuel emits a huge amount of CO_2 just in 2012, 31.6 Gt of CO_2 was released by fuel [10][11].

Renewable energy is a promising way that fits with two above-mentioned issues. Currently just only 19% of the global power production is provided by renewable energy mainly from traditional biomass (9.3%) and modern renewable energy (9.7%) such as wind, solar and hydro power [12].
Solar energy is one of these renewable energies with huge capacity to provide all of our power demand for future. Worldwide electrical power production at 2011 was 2.3×10^{12} W, while we receive 100,000 times more solar power from the sun. The capacity of this source of energy is incomparable to other terms of renewable energy and even fossil fuel and nuclear energy, which is shown in figure 2.1(b) [13].

Photovoltaics (PV) is one of the several methods to harvest solar energy by converting solar radiation to the most popular forms of energy: electricity. By only covering 40% of earth Sahara's surface (0.16% of earth's surface) by photovoltaic cell with 10% in efficiency [13], more than our current annual power consumption

could be harvested from solar power. In a sharp contrast to this huge potential of PV the total global operating capacity was 100 GW in 2012 [12], which is still less than 0.1% of the total global generated electrical power.
The main reason of this low contribution of PV in global electricity production is the cost of electricity produced by PV, which is still expensive as compared to other methods of electricity production. High efficient solar cells are too expensive and the cheap solar cells do not have sufficient efficiency to be competitive. There is still room for development and research to reduce the cost of solar electricity, either by boosting efficiency or by reducing cost of production. The other problem is unstable performance during day in which efficiency dramatically drops at cloudy weather and during night.

a) b)

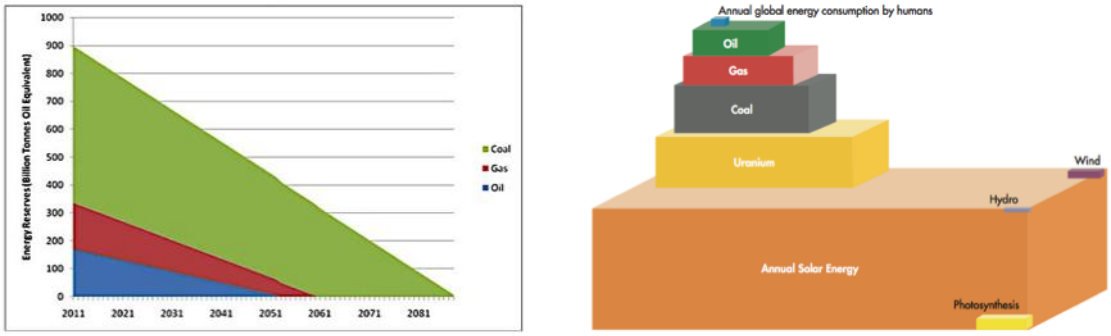

Figure 2.1: a) Fossil fuel energy reserves based on current consumption. b) Annual solar energy in comparison other energy reserves and annual global energy consumption. INTERNATIONAL ENERGY AGENCY. Energy Technology Perspective. IEA, 2008.

2.2 III-V Solar Cell

Flexible combination of III-V materials from binary to quaternary compounds, with variation in bandgap makes them suitable to be tailored for solar spectra, figure 2.2 (a) and also suitable characteristics such as high absorption coefficient, carrier mobility and large diffusion length principally make III-V materials suitable materials for most efficient photovoltaic cells [16]. III-V solar cells are also the most expensive photovoltaics, low profusion of elements (such as Ga and In) and complexity of synthesis and fabrication are the main reasons of cost [14][15].
GaAs and InP are two suitable materials for high efficient single junction III-V solar cells due to their bandgap value, which is close to the bandgap of the most highest efficient single junction solar cell based on Shockley-Queisser limit as it is illustrated in figure 2.2(b) [17].
But the biggest disadvantage of planer III-Vs is the relatively high production cost. To reduce the production cost thin film solar cells were designed and developed but suffer from complexity of growth on cheap substrate and photon absorption [21][23].

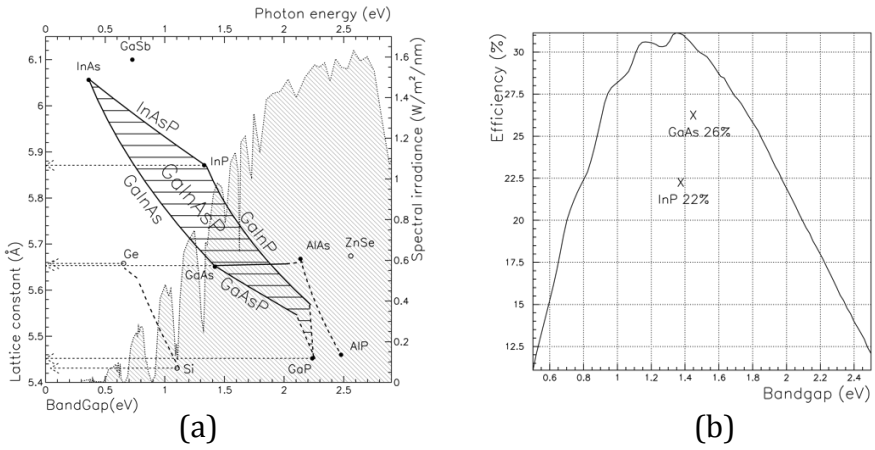

Figure 2.2: a) Lattice mismatch with relevant energy bandgap for major III-V materials in comparison with solar radiation spectra at sea level. b) Shockley-Queisser efficiency limit versus energy band gap, GaAs and InP are suitable materials for high efficient solar cell. The SolarWiki.

2.3 Nanowire Solar Cell

After planar wafer-based and thin-film solar cells, nanowire solar cells have received great interest of researchers in the last decade for next generation of solar cells. Ability of tailoring materials properties in nanoscales is one of the key motivations for this huge interest. Strong light absorption due to extreme light trapping and high scattering trough NWs with inherent anti-reflection properties [18][19], and efficient carrier collection due to small scale size and geometrical design of NWs have proved the potential of NWs solar cells to approach the standard theoretical limits with lower quantity and quality of material [20][21].

Planar single junction solar cells generally have thicknesses between 200-500 µm, and are quite thick compared to thin film solar cells especially for Si which has indirect bandgap. Consequently the diffusion region is much thicker (200-250 µm for silicon solar cells) compared to the active region [22]. High efficient planar solar cells require high quality material to have long carrier mobility and lifetime, so planar cells require much more material with high quality besides the complexity of the growth due to lattice mismatched increases severely the cost of production. Generally, NW solar cells can be designed with three different kinds of junctions; radial junction, axial junction and substrate junction [21] as illustrated in figure 2.3. Principally, radial junction has more advantages compared to axial and substrate junction due to orthogonalization of light absorption and carrier separation direction [21]. Generally the minority carrier diffusion length for radial junction NW is ~1 µm, for axial junction 2-20 µm for silicon NW, which is much smaller than for planar solar cells [23].

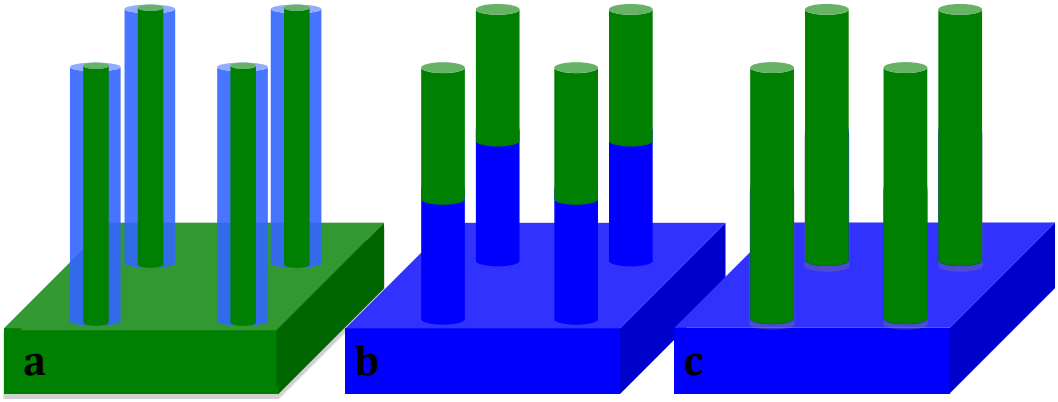

Figure 2.3: Different junction design in NW solar cells: a) Radial junction. b) Axial junction. c) Substrate junction, Blue color represents N or P type of semiconductor material and green represents the other one, P or N type

Recently it has been shown by J.Wallentin et al. that a NW array consisting of NWs with 1.5 µm length, 180 nm diameter and 12% covering area with 500 nm pitches achieved 13.8% efficiency whilst the record for planar InP solar cell is 22% [24].

NWs fulfill the requirements of low-cost high efficient solar cell in principle, which are strong light absorption and effective carrier collection while using utilizing lower quantity of material. However there are still challenges which must be overcome before commercial NW solar cell can be produced. Complexity of growth, imprecise doping control, high rate of surface recombination (due to large surface to volume ratio), uniformity of NW and stability are some of these challenges [21]. Despite research and progress in each of these areas, still much investigation and effort are needed; even if all these challenges were to be overcome, the fabrication and production technology have not been tailored for these types of solar cells in large and commercial scale.

3. NWs Transferring and Device Fabrication

3.1 Technical background

Usually high crystalline NWs are grown on the same substrate material to overcome strain induced by lattice mismatching. Materials such as GaAs and InP are quite expensive [25]. Reducing substrate cost for large-scale application, for instance solar cells, is desired. So peeling off the NWs from their original substrate and transferring them to a cheaper substrate is one the approaches to reduce the substrate cost in view of the fact that the native substrate principally can be reused for NWs growth [25]. The main transferring challenges are uniformity of NWs length after peeling with high order of transfer rate of array of NWs, while the position and orientation of each of them is maintained. Uniformity and orientation of NWs after peeling can dramatically affect the optical properties and fabrication process, which they have been designed and optimized for. Therefore keeping the NW array structure after peeling is significantly important.

Peeling the NWs with polymers has been reported, but all the reports are related to the NWs with long lengths, more than 10 μm [25][26]. The main focus of peeling in this work is to peel off much shorter NWs, about 2.5 μm in length. Geometry (length, diameter and pitches) of the NWs can affect the peeling. For instance, longer, thinner NWs with greater pitch are much easier to peel off than shorter, thicker with smaller pitch.

3.2 Peeling and Transferring Processes

To peel off NWs from the substrate they need to be embedded into a polymer with good adhesion to the NWs. Since the peeling is a mechanical process, a polymer is a good candidate due to flexibility and elasticity, preventing it from breaking and keeping the wires orientation. After peeling the NWs by use of a polymer, a back contact is applied by depositing a thin layer of metal on the backside of the membrane. The next step is bonding; the membrane is bonded to the cheap carrier substrate by bonding matrix from the backside followed by removing the membrane by either wet or dry etching. At the end the NWs should be standing up as before

ripping, with the same orientation and position as compared to each other but on the new substrate. Figure 3.1 shows the different steps of the entire procedure of this transferring technique. The procedure with all details and the used material as membrane has been described in section 3.4 Peeling Polymers.

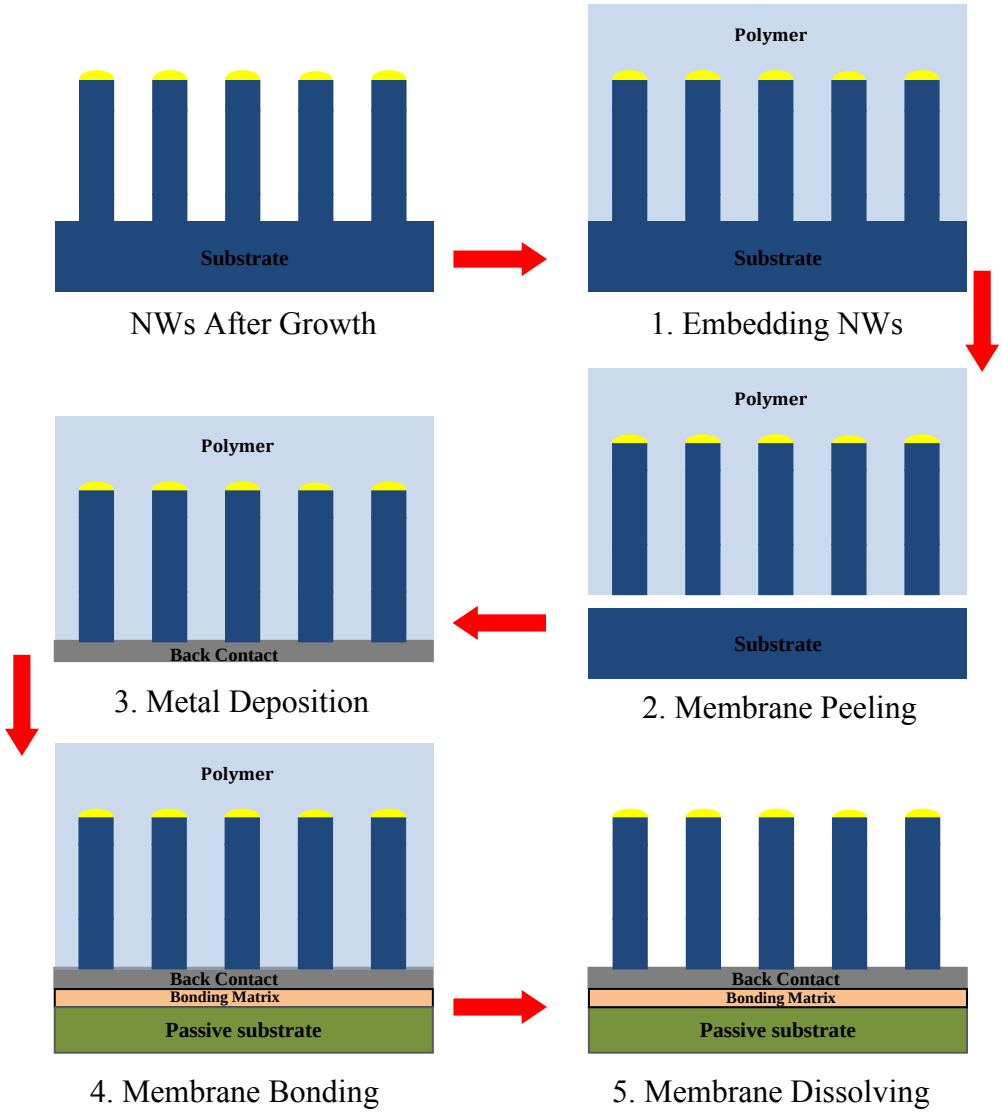

Figure 3.1: Schematic of peeling and transferring procedure. 1) First, NWs after growth are embedded into polymer. 2) Second, NWs are peeled off from the native substrate. 3) Third, back contact formation by metal deposition. 4) Next step is membrane bonding to cheaper passive substrate, such as silicon. 5) Final step is dissolving of membrane.

3.3 Device Fabrication Process

In order to make a solar cell device from the transferred NWs array, a thin layer of high-k dielectric material deposition is desired before peeling to prevent possible short circuit leakage, figure 3.2-1. After deposition, the dielectric must be removed at the tip of the NWs to make top contact, figure 3.2-2. The NWs are peeled off and transferred to the new carrier substrate as mentioned in previous part. Next is the

planarization to prevent connection between bottom and top contacts and also make NWs more stable during the process. Figure 3.2-4 shows spinning of spacer and etching it back to expose tips of the NWs. Front contact is defined by lithography followed by deposition of transparent conductive oxide (TCO) as front contact. After the lift off process TCO is deposited on the defined pad figure 3.2-5. A bond pad is defined at the edge of the front contact and deposited as a thick layer of highly conductive metal such as gold to make it possible make contact with a probe during the measurement, figure 3.2-6.

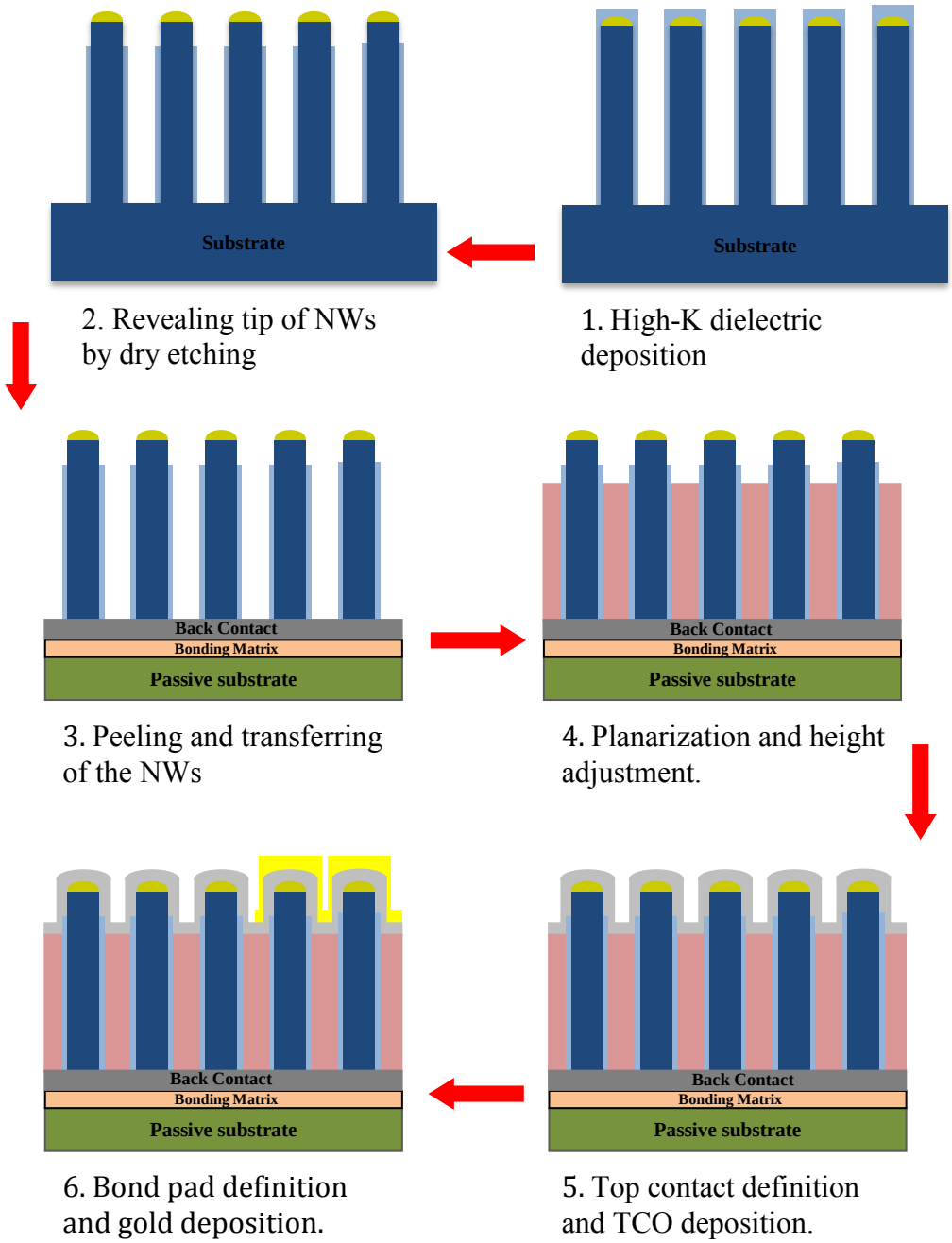

Figure 3.2: Schematic of device fabrication procedure. 1) Depositing the NWs with high-k dielectric after growth. 2) Revealing tip of the NWs by dry etching for top contact. 3) Peeling and transferring of the NWs by embedding them into membrane and bonding to cheaper passive substrate.4) Planarization by spinning spacer and etching back to expose the tip of the NWs. 5) top contact pattern definition and deposition. 6) Bond pad definition and metal deposition.

3.4 Peeling Polymers

As mentioned before, polymers are the good candidate for mechanically peeling the NWs from their native substrate due to good adhesion and flexibility. Four different polymers were used in this work to peel off the NWs, where each of them has their own cons and pros in term of adhesion, simplicity of use, flexibility and stability during processing of device fabrication (such as chemical and temperature stability). All the materials and the procedure of peeling are described in the following sections.

3.4.1 Polydimethylsiloxane (PDMS)

PDMS is an organic polymer based on Si with the empirical formula $(C2H6OSi)n$, where n is the number of repletion. PDMS is a viscoelastic material, it is liquid for low n and semi-solid for large n. It has various applications such as microfluidic device fabrication, soft lithography, device encapsulation, contact lens manufacturing and in food industry. Generally PDMS is a non-toxic, non-flammable bio-compatible material which is flexible and transparent with semi good adhesion to a wide variety of materials. In many of these application PDMS is mixed with a cross-link agent (which bonds the polymer chain together) to harden the liquid PDMS and make it a flexible solid, similar to rubber. Peeling off also requires solid phase PDMS, which is mechanically robust and can hold the wires [27][28][29].

Table 1 shows the three different PDMS and relevant agent, which were used with their physical parameters. The major difference between these two types of PDMS is viscosity; 625A is much more viscous as compared to 601A which makes it a good material to peel off short NWs while it has 6 times higher elongation. But it is not really a good candidate to peel off long NWs since it cannot penetrate all the way down trough to the substrate as will be shown later.

Product name	Curing agent	Mix ratio A:B (pbw)	Viscosity at 23 °C, mixed (mPa s)	Elongation at break (%)	Tensile strength (N/mm^2)
ELASTOSIL ® RT 601 A	ELASTOSIL ® RT 601 B	9:1	3500	100	6.0
ELASTOSIL ® RT 625 A	ELASTOSIL ® RT 625 B	9:1	25000	600	6.5
SYLGARD® 184	SYLGARD® 184 (agent)	10:1	5000	Not determined	Not determined

Table 1: Comparison of three different PDMS, which were used in this work

The preparation procedure is quite the same for both of the mentioned products. After mixing PDMS and its relevant agent with weight ratio of 9:1, it was necessary to stir the mixture carefully to make the curing agent distribute uniformly. To eliminate trapped air bubbles, which can be introduced during stirring, a vacuum-connected desiccator was used to leave the mixture in it for 30 minutes. In order to spin on PDMS, all the samples were bonded on one-inch Si wafer by crystal bonding to make it easier to place them on the spinner chuck. After dropping mixture droplets on the samples and waiting for 2 minutes to allow the mixture fills out the space between the

NWs and go between the wires completely spinner was used at rotational speed of 800 rpm with ramp stage 300 for 30 s to obtain an even 100 µm film of PDMS. All the samples were placed in an oven at 80 °C for 1 hour to cure the PDMS. The curing time is highly dependent of the temperate and PDMS thickness; generally for higher temperature shorter curing time is required. Afterward, the PDMS membranes were peeled off with tweezers, and the NWs embedded into the membrane followed with high rate.

It was found out that for PDMS 601A the critical length for peeling is ~ 2µm, as it is shown in figure 3.3. InP NWs with 2 µm length and 180 nm diameter were peeled off just at bottom part. Backside images from membrane show that the NWs maintain their orientation and position with respect to each other. (Since the membrane is not conductive, it is hard to image the samples without charging).

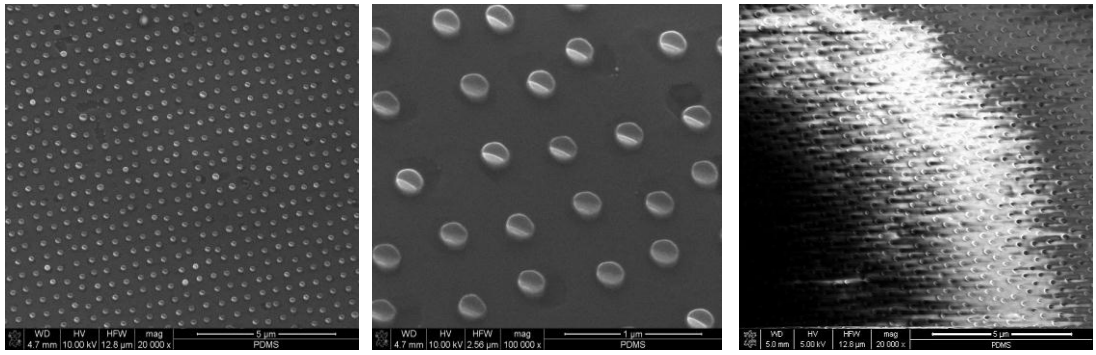

(a) (b) (c)

Figure 3.3: a,b) SEM images at 30° tilt of the substrate after peeling with PDMS 601A, InP NWs array with D = 180 nm, L = 2 µm were peeled of from substrate. c) SEM image at 45° tilt of backside of membrane after peeling; the dots indicate the bottom of NWs.

To peel off shorter NWs PDMS 625A and its relevant agent 625B were used; since it has better adhesion and tensile strength it will not tear off during the peel off while it sticks to NWs. After embedding the NWs into the PDMS and before peeling the membrane, tweezer was used (it could be any other thing that doesn't have sharp edge to tear PDMS) to gently swipe on top of PDMS to break off the NWs from their base. Figure 3.4 shows the NWs array with 1.1 µm length and 138 nm diameter before and after peeling.

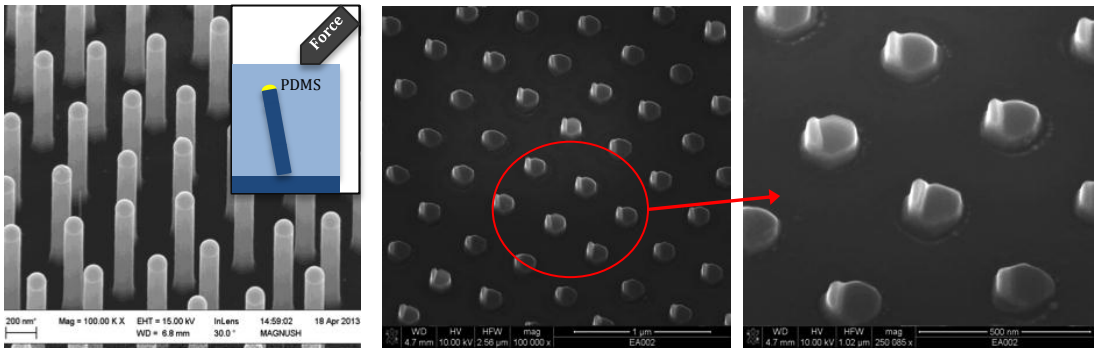

(a) (b) (c)

Figure 3.4: a) SEM images at 30° tilt of an InP NWs array with D = 138 nm, L = 1.1 µm after growth, inset: schematic of the method of breaking the NWs from the base. b,c) SEM image at 30° tilt of the substrate after peeling, showing that all the NWs were broken at the bottom part

3.4.2 SolOne™

The second polymer that was used to peel off NWs in this work it is SolOne™, which was provided by Sol Voltaics AB Company. Due to proprietary information agreement it is not possible to define exactly that the material properties, but generally it is a liquid phase of material, which is basically a mix of two different components, a polymerizable component and a solvent component. The solvent component, which is mainly Acetone and Ethanol, maintains the solution in liquid phase but after solvent evaporation it will be polymerized. The final polymer is very similar to Delrin (Polyoxymethylene).

Experimental investigation demonstrates that SolOne™ has higher adhesion (after polymerization) as compared to PDMS and lower viscosity (it has not been determined, but is in liquid phase compared to PDMS which is in liquid/viscous phase), which helps to penetrate between the NWs array and consequently peel off NWs with higher yield of transferring. The peel off procedure with SolOne™ is easier than using PDMS since there is no need to prepare the SolOne™ by mixing the materials; it is already prepared and does not have the trapped air bubbles which is inevitable during PDMS preparation. It is just necessary to drop a couple of droplets or spray SolOne™ on the samples and let it dry out for more than 12 hours. The peeling part it is exactly same as for PDMS. As it is mentioned in section 3.2 and 3.3 after bonding the membrane itself must be removed to make it possible to further process and fabrication. Due to Lund Nano Lab's restriction it is not allowed to dry etch both of these polymers with Reactive-ion etching. Chemical etching to dissolve PDMS with its relevant solvent Dynasolve 210 is forbidden in the clean room. SolOne™ is allowed to be used in Lund NanoLab clean room as well as the its relevant chemical-etching solvent (Thinner). Furthermore, bonding the membrane to the carrier substrate for further process and device fabrication is another problem of using PDMS. By considering all these issues, SolOne™ was chosen as a main material to peel off the NWs and subsequently to fabricate the solar cell device from peeled off NWs. During peel off experiment and developing the technique with SolOne™ it was discovered by experimental evaluation of several samples with varying NW length that the critical length to peel off the NWs is about 2.2 μm for diameter 150-200 nm.

Three samples with the same NWs array dimensions were used to investigate the capability of each of these three polymers for peeling purpose. Samples with NWs dimension: 2.7 μm length and diameter varied from 600 nm at the top of the NW to 500 nm at the bottom with 1000 nm in pitch were prepared to be peeled off by the use of PDMS 601, 625 and SolOne™ separately. After peeling, all the substrates were inspected by SEM to compare the results. Figure 3.5 shows the substrates after peeling; as indicated, the top two images (a,b) relate to the sample was peeled off by PDMS 601. The dark area at top left image (indicated by red circle) is the peeled off NWs and the bright area is the NWs that have not followed along during peel off. The same phenomenon is observed for use of PDMS 625, as shown in figure 3.5(c). Most of the NWs were not peeled off, and were found still standing on the substrate. By imaging with higher magnification it was observed that PDMS 625 was stuck at middle along the NWs due to higher viscosity as compared to PDMS 601 that penetrated all the way down to the bottom of the NWs but had not enough adhesion to

NWs to peel them off. With SolOne™ peel off was successful as shown in figure 3.5(e), which shows the substrate after peeling. Figure 3.5(f) is related to the NWs embedded in membrane; the array structure of NWs has been maintained.

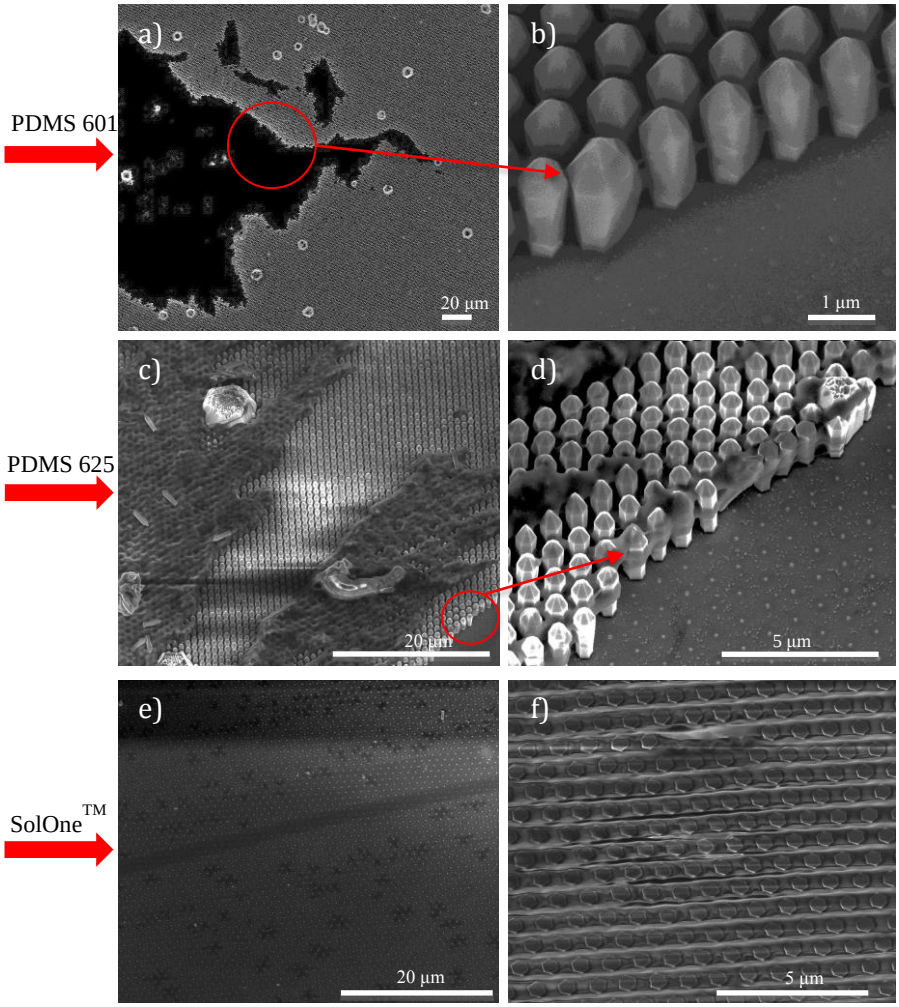

Figure 3.5: a,b) SEM image of the substrate after peeling by PDMS 601, most of the NWs were left on the substrate although the PDMS 601 penetrated between the NWs all the way down. c,d) SEM image of the substrate after peeling by PDMS 625, peeling was poor since PDMS 625 could not penetrate to the bottom. e) SEM image of substrate after peeling by SolOne™; all the NWs were peeled off nicely from the bottom. f) SEM image of backside of the SolOne™ membrane after peeling.

3.5 Bonding Matrix

After peeling off the membrane and depositing metal on the backside, it must be bonded on the carrier substrate to be easy to handle and to withstand during further device fabrication processes such as spin coating, heat-curing, chemical developing and lift-off. The bonding matrix material must be compatible with mentioned fabrication process steps. The main challenges to find appropriate bonding matrix are adhesion, flatness, temperate and chemical stability. Good adhesion to the metal is

desired since after peeling and metal deposition, the membrane should be bonded to the bonding matrix from the metal side.
Discrepancy in length of the NWs after transferring can affect the process step mainly spin coating to get uneven, and subsequently can affect the planarization and contact deposition so flat bonding of membrane is needed. Samples need to be baked at a temperature of 200^{o} C, or chemically developed in some step of the device fabrication process, so temperature and chemical stability of the bonding matrix is needed.

The investigation was done on different conventional and available material to find out the suitable bonding matrix for this work based on the possible chemicals, used for fabrication. Table 2 shows the result of an experimental investigation of chemicals and different steps of the fabrication. Since after bonding the membrane has to chemically dissolve (it is not allowed to use the dry etch to etch thick amount of materials in the LundNanoLab), and the membrane used in this work is SolOne^{TM}, its relevant chemical dissolver thinner is also included in the investigation. Remover 1165 and developer MF319 are also chemicals used during the fabrication process for lithography, development and lift-off.

Bonding Matrix	Thinner (SolOneDissolver)	Dynasolve 210	Remover	Adhesion to Membrane	Heat Resistivity	Flatness
PMMA	Can't Stand	Can't Stand	Can't Stand	Poor	Good	Good
S1813	Can Stand	Can't Stand	Can Stand	Poor	Good	Good
Uncured BCB	Can't Stand	Can't Stand	Can't Stand	Good	Good	Good
Cured BCB	Can Stand	Can't Stand	Can Stand	Poor	Good	Good
Ag Paste	Can't Stand	Can't Stand	Can't Stand	Good	Good <150°C	Poor
In Droplet	Can't Stand	Can't Stand	Can Stand	Good	Good <100°C	Poor
Cured PDMS	Can Stand	It is used for removing PDMS	Can Stand	Very Good	Good	Poor
Imprint Resist	Can Stand	Can't Stand	Can't Stand	Good	Good	Good
Super Glue	Can't Stand	Can't Stand	Can't Stand	Good	Poor	Poor

Table 2: Result of investigation on potential materials as a bonding matrix

PMMA, S1813, BCB, Imprint Resist and PDMS were spin-coated with spinner on the carrier substrate to achieve really flat surface, which was not possible for others. To check heat resistivity of the bonding matrix, all of them were ramped up to 200^{o} C to observe if they can stand that temperature. Adhesion was also experimentally checked, membrane from metal deposited side was put on top of the carrier substrate with bonding matrix to observe if membrane will attach to bonding matrix or not. All the carrier substrates with different bonding matrix were separately put in the remover and then thinner to see if they are not dissolving. Some of the bonding matrixes have to be baked such as BCB and S1813, since makes the adhesion very poor after baking. After all the these experiments PDMS was chosen as a bonding matrix although it was not the really suitable material for bonding matrix but it was the only and most compatible material to our process.

3.6 Ohmic Contact

Semiconductors have received interest for optoelectronic and high-speed electronic devices, such as solar cells, light emitting diodes and transistors. One of the main challenges to achieve a high device performance is formation of ohmic contact between the semiconductor and the metal, which in principle means that the contact resistance will be low, and that charge carriers can flow from semiconductor to metal and vice versa [30]. Generally ohmic contact to intrinsic semiconductors is difficult due to a difference between metal and semiconductors work function [31], which results in band bending and built in potential barrier at the metal-semiconductor interface called Schottky barrier, figure 3.6(a). The height of the barrier can be calculated by the Schottky–Mott rule to be difference between metal work function and semiconductor electron affinity [31]. A large number of surface energy states at semiconductors surface and consequently Fermi level pinning makes the barrier height partially independent of the metal and semiconductors work function. The common techniques to make ohmic contact to the semiconductors are; selecting a metal with appropriate work function, inserting the material with narrow gap between metal and semiconductors and increasing doping level at semiconductors surface. Increasing doping level ($N_D > \sim 10^{18} cm^{-3}$), the depletion-layer width becomes narrow ($W_d < \approx 2.5–5nm$) so electrons can "tunnel" through the potential barrier due to the wave nature of electron, figure 3.6(b). Generally, ohmic contact fabrication to p-type semiconductor is even more difficult than to n-type, because the larger holes effective mass as compared to electrons, which limits hole transport properties since probability of tunneling for holes with larger effective mass is lower than for electrons with smaller effective mass [32]. For some materials for instance GaAs ohmic contact to p-type is easier than n-type properties.

Ohmic contacting to the NWs after peeling is desired but has not been investigated during the course of this work. The conventional Ti/Au/Ti metal contact is deposited by sputtering on the backside of the membrane as a back contact. A thin layer of Ti is used due to poor adhesion of gold (Au) to polymer surface and Ti is preventing the gold from spiking by diffusing into the semiconductor. Again after Au a thin layer of Ti is deposited for outer layer to take the advantages of Ti adhesiveness to attach the membrane to the bonding matrix.

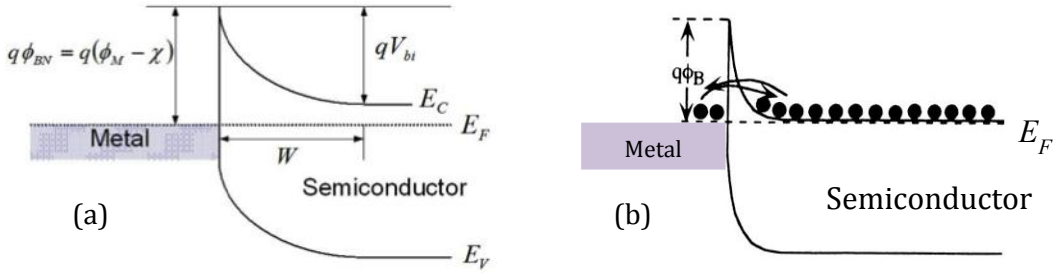

Figure 3.6: a) Metal semiconductor interface causing built-in potential (V_{bi}). b) Ohmic contact formation by increasing doping at semiconductor surface making the junction thin enough for electron tunneling.

4. Results and Discussion

In this work three different types of measurements and investigations were done including photoluminescence on peeled NWs, absorption trough embedded NWs array and device fabrication from peeled off NWs. Each measurement is described individually by first induction and technical background of the measurement followed by procedure of the measurement and discussion about the result.

4.1 Photoluminescence (PL)

4.1.1 Introduction

One of the common methods to study electrical and structural properties of materials is photoluminescence (PL) characterization since it is contactless, nondestructive and also faster than conventional electrical measurements. As simple explanation of PL operation, the sample is irradiated by a light source (mostly laser with certain energy) then luminescence of the sample is measured [33]. PL measurement can characterize properties such as carrier concentration, minority carrier lifetime, bandgap, crystalline quality, impurity levels and defect states.

For direct bandgap semiconductors, typically a laser with low wavelength is used to provide photons with energy higher than the semiconductor bandgap. By absorbing the photons electrons are excited from the valance to the conduction band and electron-hole pairs with same momenta will be generated [34]. Generally, these generated electrons and holes after releasing some portion of their energy trough nonradiative processes (mostly phonon scattering) will thermalize to the local ground state where they finally recombine. This process happens when the relaxation time is shorter than the recombination time. Since the probability of radiative recombination is higher than nonradiative recombination in direct bandgap semiconductor, photons with energy equal to the energy difference of recombined carriers will be emitted. Figure 4.1 shows the PL mechanism.

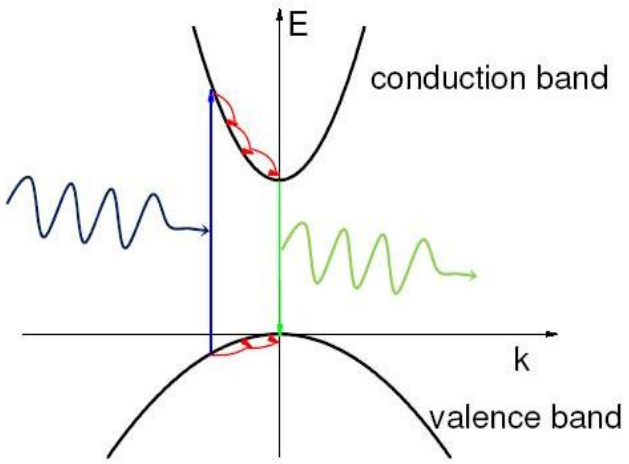

Figure 4.1: Photoluminescence mechanism; an incident photon is absorbed and excites electron to conduction band (blue). After relaxation and releasing excess energy (red), generated carriers recombine and emit a photon.

One of the challenges for PL measurement on NW is the substrate contribution especially when substrate and NWs are the same material. That makes it hard to study NWs PL data due to the effect of the substrate peek on NWs peek. Peeling the NWs from the substrate embedding them in a polymer film for characterization allows overcoming this problem and also makes it possible to do PL at the bottom of the NWs to get some information about bottom part of the NWs, which is hard while they are standing on the substrates.

4.1.2 PL measurement and Results

Some samples with InP NWs were provided for investigation of PL measurement on embedded InP NWs after peeling. Figure 4.2 shows the optical setup used for room temperature PL measurement on the membrane after peeling the NWs from the substrate. PL measurements were done on the sample while the NWs were standing on the original substrate (before peeling), on both sides (top and bottom) of membrane and on the substrate after peeling.
A laser with 375 nm wavelength and 15 mW power was used as light source. To prevent the membrane from burning and damage due to the laser power, optical filters were used to decrease the intensity of the incident light. Laser light was sent trough the regular microscope to make it possible to focus the light on the membrane. The same microscope was used to collect the portion of emitted photons and carry them to detector by optical fiber. The detector was connected to computer and BWspec 3.25 software was used to adjust the measurement parameters and observe the results.

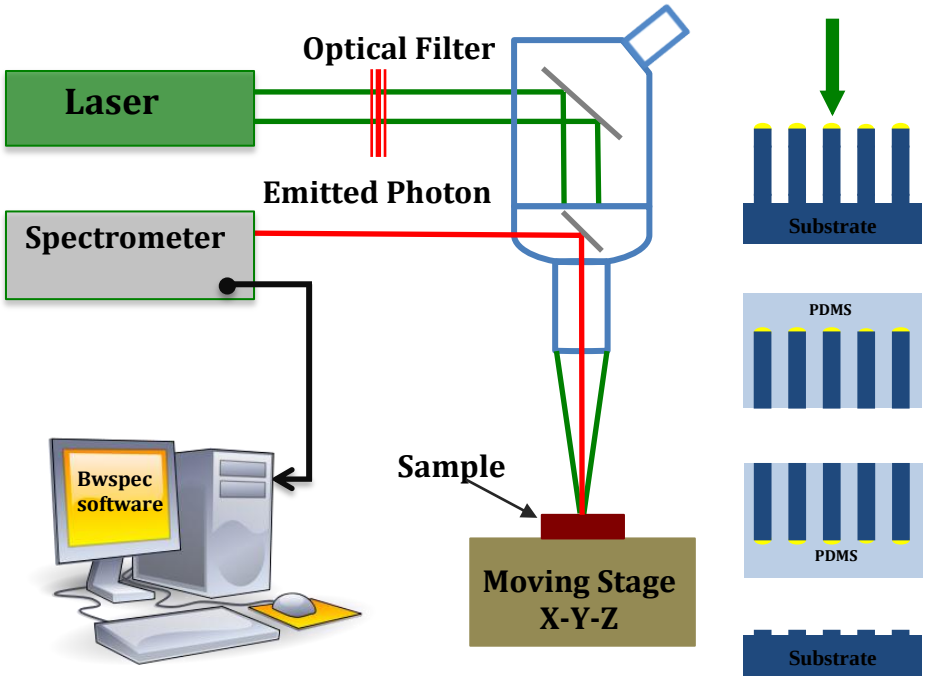

Figure 4.2: Schematic of PL set up; PL was done on NWs after growth while standing on the native substrate. PL was also performed on the top and bottom membrane sides as well as on the substrate after peeling.

Figure 4.3 shows PL spectra of two different samples from same growth but different NWs lengths; each color of PL spectra is related to an individual different measurement. The blue spectrum is related to the sample after growth when the NWs were still standing on the substrate. Red and black spectra are related to PL measurement on the both sides of membrane, top and down, respectively after peeling. The green spectrum is related to the substrate after peeling.

Both samples show the main peek around 1.4 eV for PL measurement on the NWs while standing on substrate, which is related to the InP bandgap with wurtzite structure at 300 K. As it is shown the peaks are not quite sharp and the spectra show some shoulders (smaller peaks) at lower and higher energy for both of the samples. PL on top of the membranes also shows the same peek at 1.4 eV but with smoother spectra for higher energy. By flipping the membrane, PL was done on the backside of the NWs. The shoulder at lower energy was observed to be intensified for both of the samples; for the sample with longer NWs length that intensification was more significant, figure 4.3(b). The peak at lower energy was detected at 1.35 eV, which is close to the InP bandgap for zincblende structure at room temperature. That indicates that the wires have been grown with two different crystal structures (zincblende and wurtzite) especially with a zincblende structure at the bottom part of NWs. PL on the substrate after peeling showed a peek at 1.44 eV, which indicates the highly N-type InP substrate.

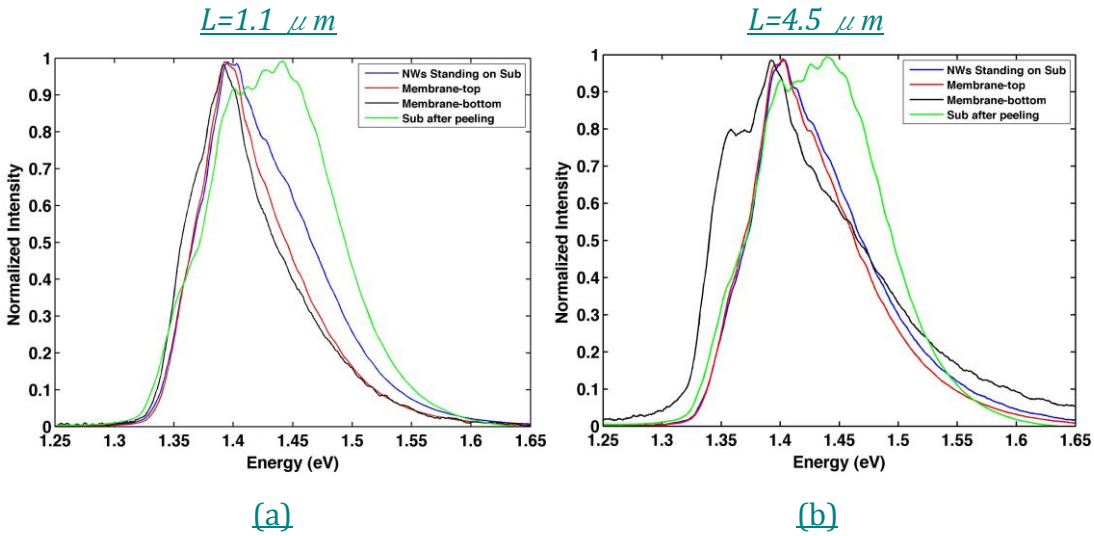

Figure 4.3: PL spectra for NWs standing on substrate (blue), top and bottom of the membrane after peeling (red, black respectively) and substrate after peeling.

4.2 Absorption Measurement

4.2.1 Introduction

Reflection and transmission prevent optimum absorption; some portion of light is reflected back by the semiconductor surface, and also some portion is transmitted trough the semiconductor. Sufficient thickness of each semiconductor material is required to absorb all the non-reflected light and decrease the transmission loss. To increase the thickness more material is needed which results in cost increase. Anti-reflection coating by depositing a special thickness of dielectric martial on the semiconductor surface and light-trapping effects by texturing the front and rear surface, are two common methods to reduce reflection and transmission losses respectively [35][36][37]. As mentioned before NW arrays are promising for photovoltaics applications due to light coupling into NWs array, and anti-reflection properties that results in strong light absorption.

Extensive studies about NWs optical properties have demonstrated the strong light absorption in ordered array of NWs [38][39][40]. Due to benefit of scatting, resonance and diffraction effects in ordered array of NWs the light path length will increase and result in strong absorption [41][42]. These optical properties are highly

dependent on the geometrical size of NWs array such as length, diameter and pitch. There are also some experimental reports about light absorption into NWs, but all of that have been measured while the NWs were standing on their substrate, which makes analysis of the experiment more complex due to contribution of the substrate. By peeling off the NWs array from the substrate while the orientation is kept, it is possible for direct experimental investigation of light absorption trough the NWs array embedded in transparent membrane.

In this work, an experimental study about light absorption of InP NWs array with varying NWs diameter and length has been done. For the experimental investigation, two series of the samples were grown, one with length variation and the other one with diameter variation to study the effect of NWs dimension on their light absorption.

4.2.2 Measurement and Result

The NWs have been grown with the particle–assisted MOVPE method. For the length series samples with different lengths of NW were grown by increasing the growth time. For the diameter series, the gold particles were removed and different thicknesses of shell were grown by increasing the time in order to get different diameters. Figure 4.4 shows the simple schematic of the growth procedure.

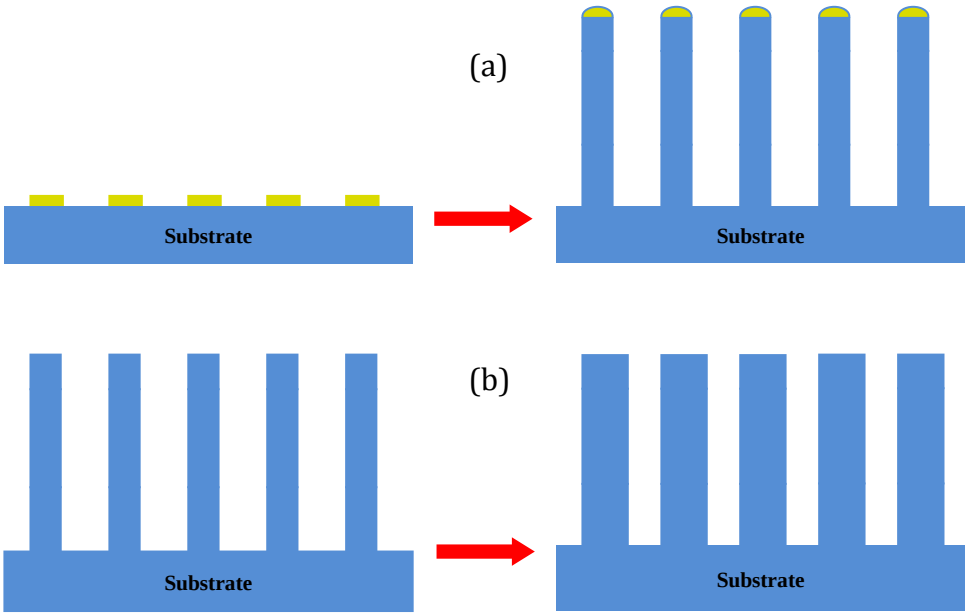

Figure 4.4:a) NWs growth by particle–assisted MOVPE method. Increasing the growth time longer NWs are harvested. B) After removing Au particle, increasing laterally growth time result in thicker NWs.

SEM inspection was done for each sample, to determine the average diameter D, length $L_{\text{as-grown}}$ and their corresponding standard deviation by measuring the diameter and length of 50 grown NWs as it is shown at figure 4.5(a). Then NWs arrays were embedded into PDMS 625 and peeled off from the substrate. To determine the actual length of NWs embedded to PDMS membrane, all of the substrates after peeling were inspected with SEM to measure the average length of NWs left part L_{sub} on the substrate, figure 4.5(b). Then, the NWs average length L in the PDMS membrane was calculated as $L = L_{\text{as-grown}} - L_{\text{sub}}$. And the final standard deviation (SD) of the actual length of embedded NWs was measured by $SD = [SD_{as\text{-}grown}^{2} + SD_{stub}^{2}]^{(1/2)}$, ($SD_{as\text{-}grown}$=standard deviation before peeling. SD_{sub}=standard deviation of left part on the substrate). In the quoted values, the uncertainty denotes the standard deviation in length and diameter.

A sample from diameter series shows dual diameter in which the lower part of the NWs was thinner with constant diameter around 135 nm for all of the sample and the upper part was thicker and increased by increasing laterally time growth, Figure 4.5(c). Figure 4.5(d) shows one of the membranes with embedded NWs after peeling.

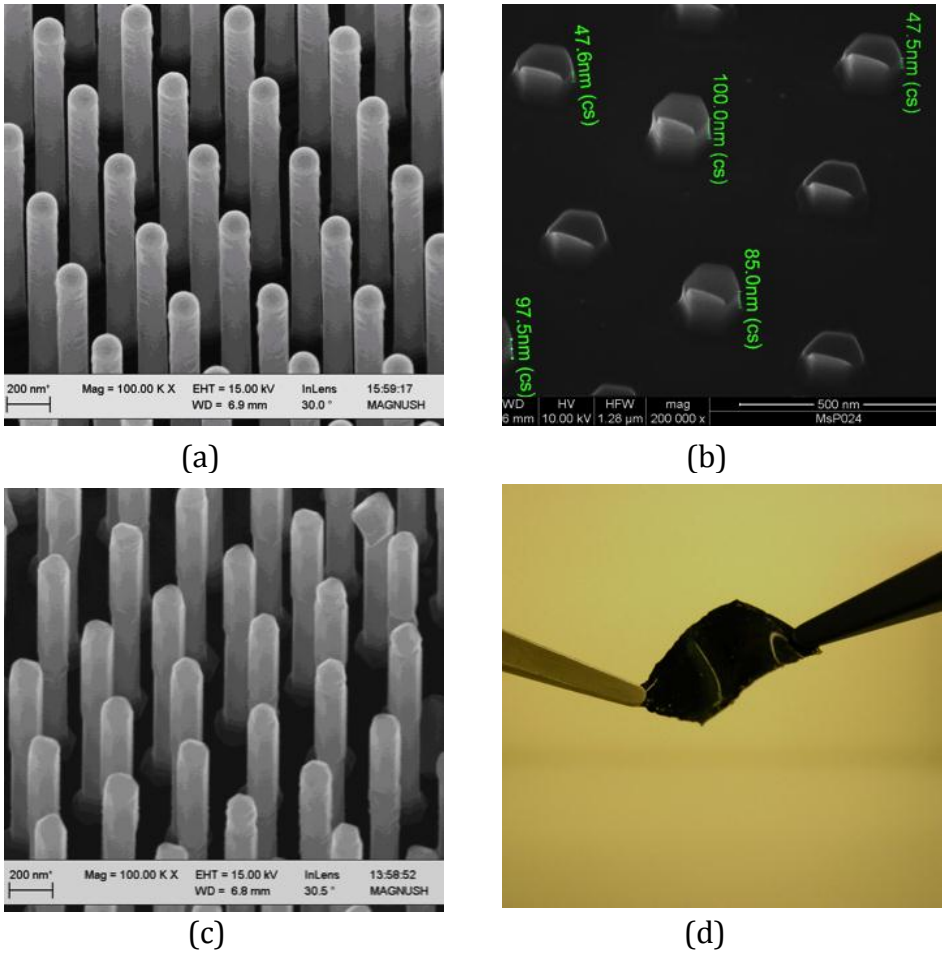

Figure 4.5: SEM image at 30°. a) NWs after growth while standing on native substrate. b) Substrate after peeling, inspection was done to check the quality of peeling and measure length of probable left part on the substrate to be deduced from the length after growth. c) A sample from the diameter series with dual diameter geometry, thicker at the top. d) Optical images of membrane with embedded NWs after peeling.

SEM inspection was done for the all the samples as mentioned and the length and diameter of the embedded NWs into membrane was calculated. Table 3 and 4 show the exact embedded NWs length and diameter for both series.

Sample ID	Length before peeling (nm)	Length after peeling (On substrate (nm)	Final Length (nm)	Diameter (nm)
AX7042	1062±19	84±30	978±35	132±10
AX7031b	1664±15	30±12	1634±19	138±4
AX7031a	1921±31	52±26	1869±40	138±4
AX7033b	1862±22	39±15	1830±27	141±3
AX7025	2275±40	190±77	2085±77	129±3
AX7032a	2322±34	73±31	2249±47	132±3
AX7028	3094±94	227±111	2867±145	138±2
AX7035a	4704±60	170±75	4534±96	147±4

Table 3: Length series NWs dimension

Sample ID	Length before peeling (nm)	Length after peeling (On substrate) (nm)	Final Length (nm)	Diameter (nm)
AX7039a	1598±24	38±9	1560±26	132±3
AX7037a	1520±40	50±10	1470±41	157±6
AX7036a	1653±87	45±7	1608±87	181±11
AX7038a	1663±83	110±26	1553±86	241±13
AX7040a	1561±67	41±23	1520±70	347±34

Table 4: Diameter series NWs dimension

To measure the total absorption of the NWs, the total reflection $R(\lambda)$ and total transmission $T(\lambda)$ were measured separately in order to calculate the absorption of the embedded NWs as:

$$A(\lambda) = 1 - R(\lambda) - T(\lambda)$$

In order to measure the reflection and transmission an integrating sphere was used as a light collector. The sphere interior surface is coated by highly reflective material so after (transmitted/reflected) light enters the sphere through the illumination port, after multiple reflections, it is scattered uniformly around the interior of the sphere. The detection fiber optics at the side of the sphere collects the light trough baffle, which prevents first reflections to enter the detection fiber. Then light is carried to the detector by optical fiber. The Measurement setup was including *AvaSphere-30-REFL* (integrating sphere), *AvaLight-HAL* (white-light source) and *AvaSpec-ULS364* (spectrometer). Figure 4.6 shows the schematic of the integrating sphere, and the reflection and transmission measurement.

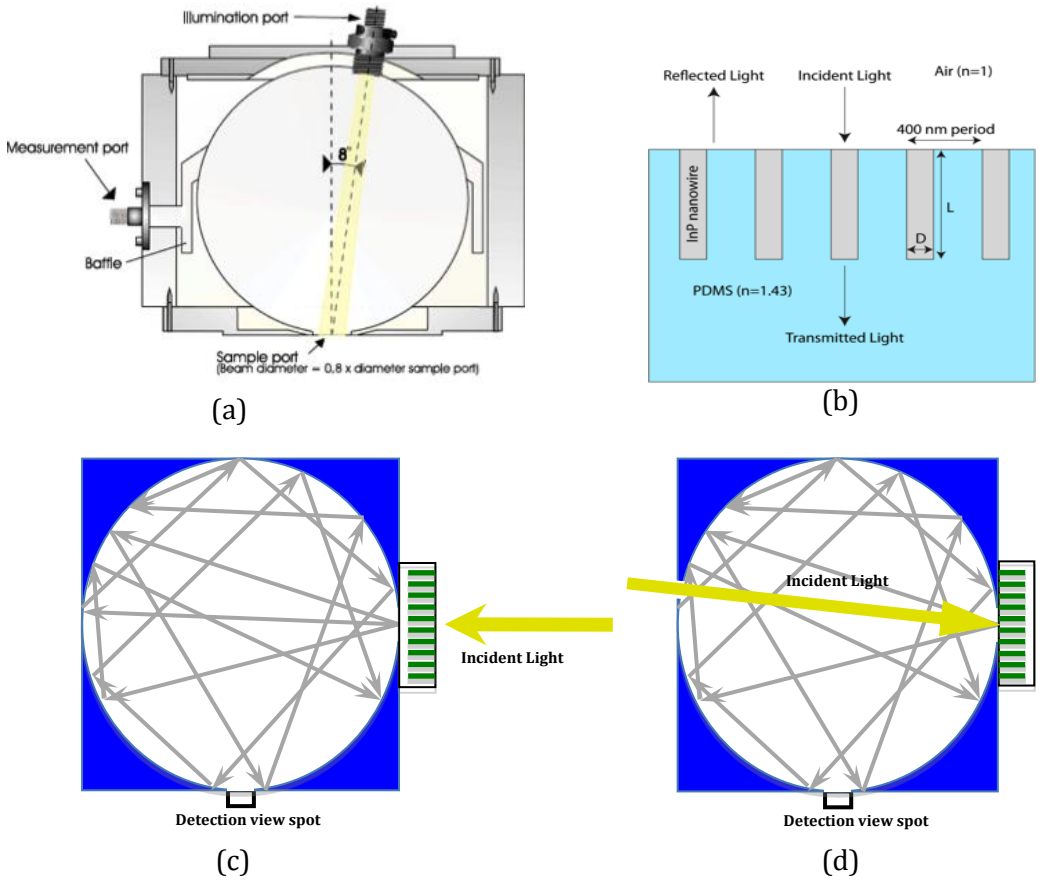

Figure 4.6:a) Cross section of integrating sphere *AvaSphere-30-REFL.* b) Schematic of InP NWs embedded in PDMS. Modeling was done when air-NW/PDMS interface was illuminated. c, d) Schematic of transmission and reflection measurement respectively

For the reflection measurements, light was sent into the sphere through the illumination-port toward the sample, which is attached on the sample view-port, and the reflected light was collected by the sphere and carried to the spectrometer. A Planar silicon substrate was used as reference for calibration and normalization. The background was calibrated by identical measuring but without any sample. During the measurement the unattached side of sample was facing to the roof of the lab to prevent back reflection of transmitted light trough the membrane. For the transmission measurement, light was sent from outside the sphere toward the sample view-port with the same focus as for the reflection measurement, and transmitted light was collected and carried to the spectrometer. The reference level was measured when no sample was attached to sample view-port, and the background level was measured without any illumination.

The measurements were performed at the very dim room (to minimize the background counts and noise) in the wavelength range of $400 < \lambda < 900$ nm with a wavelength step of $\Delta\lambda = 0.35$ nm using a 15×10^3 ms integration time both for the reflectance and transmittance measurements. In both measurement, approximately $1 \times \pi$ mm^2 in area was illuminated at the middle of the membrane (where all the SEM inspection and length and diameter measurement were done), roughly $1.2\text{x}10^7$ NWs were illuminated during the measurements. The incident light angle was kept approximately 8° for both measurements. The upper limit range of the measurement

was chosen to 900nm due to high signal to noise ratio of the spectrometer (silicon detector) above that range, which coincidentally matches nicely the band gap of InP which corresponds to a wavelength of 925 nm

Figure 4.7 shows the reflection, transmission and absorption spectra all together for some samples. Figure 4.7 (a) and 4.7 (b) illustrate the spectra for shortest (L=978±35 nm) and longest (L=4534±96 nm) samples of the length series respectively. As it is shown, the reflection level of both samples is approximately the same, but there is a difference in the transmission spectra. The sample with shorter NWs shows the lowest transmission around 630 nm (due to diameter-dependent resonance absorption) [38][40]. In contrast, the sample with longest NWs almost no light was transmitted below 700 nm and the absorption has saturated at a value of approximately 95 % for λ < 700 nm. Analyzing the reflection spectra revealed that absorption is limited by a spectrally independent reflection loss of 5 %, which we attribute to reflection at the air/PDMS interface, see figure 4.6(b).

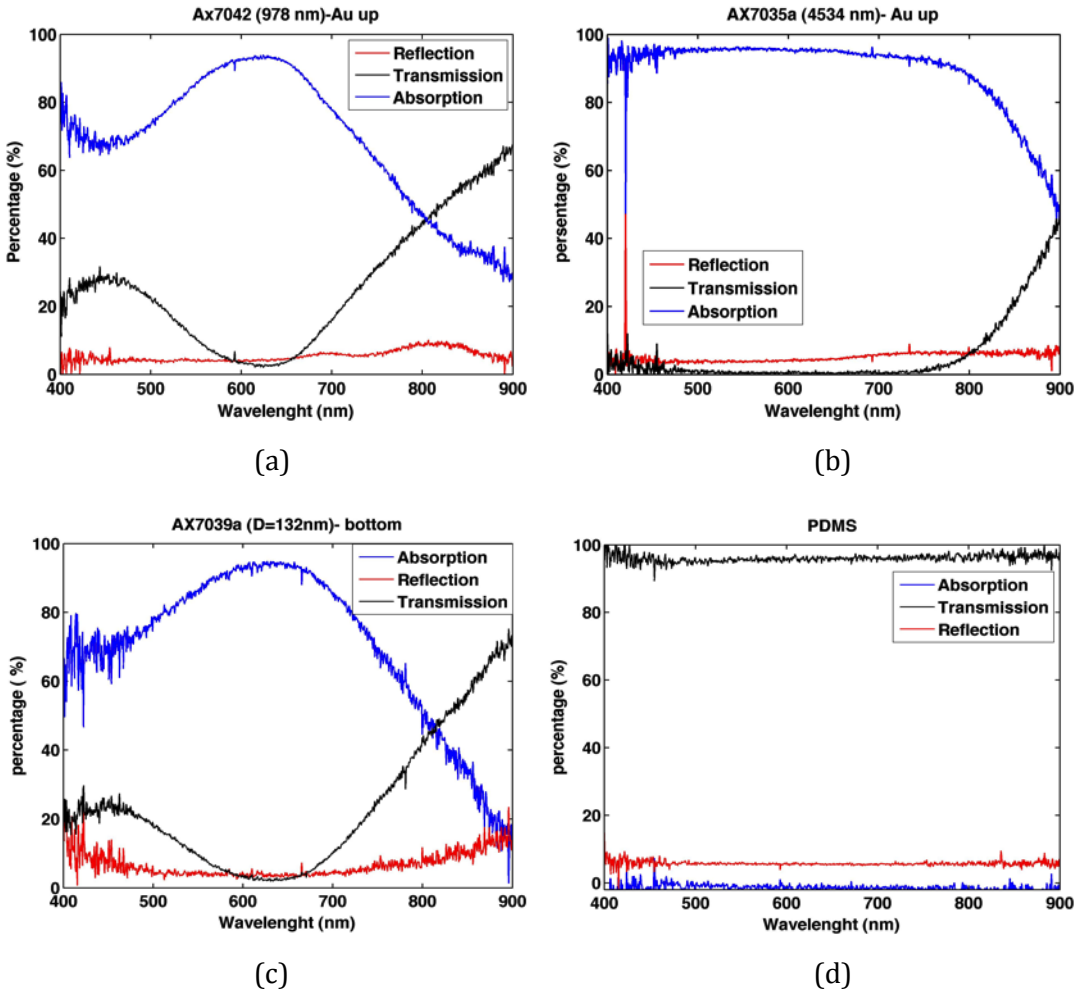

Figure 4.7: Absorption, transmission and reflection spectra a) for embedded NWs with L= 978 nm and D=132 nm b) for embedded NWs with L= 4534 nm and D=147 nm c) for embedded NWs with L= 1560 nm and D=132 nm d) The membrane without embedded NWs (PDMS 625).

The figure 4.7 (c) shows the spectra of the sample with thinner NWs diameter D=132±3 nm and length L=1598±23. The same diameter-dependent resonance absorption was observed at $\lambda \approx 630$ nm. The measurement was done also in the pure PDMS 625 (membrane without embedded NWs) to make sure that it is transparent and the membrane absorbs no light. As is illustrated in figure 4.7 (d), the absorption level of the membrane is zero. Since for the length series the gold particle had been not removed, measurements were done on both sides of the membrane (top of the NWs with gold particle and bottom of the NWs without gold particle were illuminated) to investigate the effect of the gold particle on the light absorption.

To systematically study the effect of the NW length on the absorption, the average of $A(\lambda)$ in the interval 400 nm < λ < 900 nm was calculated for all of the length series samples. Tables 5, 6 and 7 show the calculated mean value of absorption, transmission and reflection measurement respectively for each sample from the length series. First we find a rapid increase from $A_{mean} \approx 70$ % to $A_{mean} \approx 85$ % when the NW length is increased from the shortest length of $L \approx 1000$ nm to $L \approx 2000$ nm. However, the increase is less rapid for $L > 2000$ nm, and a further increase of the NW length to 4500 nm increases A_{mean} by just 0.06 to 91 %. This can be understood from the saturation of the absorption with increasing length of the NWs, figure 4.7(b).
For all of the samples reflection was about 5% when the top of the NWs (mentioned top up in the table) was illuminated by the light source, which is reasonable since all of them have almost the same diameter, and around 3% when the backside of the membrane was illuminated (mentioned top down in the table). The difference between the reflection mean values experimentally demonstrates the effect of the gold particle, which is highly reflective material on top of the NWs. For transmission measurements this difference between the two sides of the sample was not observed. The difference between two sides of the samples at reflection measurement is the main reason of the difference between top up and top down for the calculated absorption values.

Sample ID	Embedded NWs Length (nm)	Diameter (nm)	Absorption top Up (%)	Absorption top Down (%)	Difference top up & down
AX7042	978±35	132±10	68.47%	70.11%	2.34%
AX7031b	1634±19	138±4	79.98%	82.45%	3.00%
AX7031a	1869±40	138±4	75.58%	77.15%	2.03%
AX7033b	1830±27	141±3	81.73%	84.22%	2.96%
AX7025	2085±77	129±3	77.99%	79.77%	2.23%
AX7032a	2249±47	132±3	79.06%	80.44%	1.72%
AX7028	2867±145	138±2	85.54%	86.90%	1.57%
AX7035a	4534±96	147±4	89.31%	90.87%	1.72%

Table 5: Mean value of the absorption of each sample when top and bottom of the membrane is illumitated from Length series

Sample ID	Transmission Top Up (%)	Transmission Top Down (%)	Difference top up & down (%)
AX7042	26.18%	26.08%	0.38%
AX7031b	14.30%	14.15%	1.06%
AX7033b	12.45%	12.16%	2.38%
AX7031a	18.89%	19.06%	0.89%
AX7025	16.59%	16.34%	1.53%
AX7032a	15.54%	15.60%	0.38%
AX7028	9.11%	9.23%	1.30%
AX7035a	5.63%	5.73%	1.75%

Table 6: Mean value of the transmission of each sample from Length series

Sample ID	Reflection Top Up (%)	Reflection Top Down (%)	Difference top up & down (%)
AX7042	5.35%	3.81%	28.79%
AX7031b	5.72%	3.40%	40.56%
AX7033b	5.82%	3.61%	37.97%
AX7031a	5.53%	3.79%	31.46%
AX7025	5.42%	3.89%	28.23%
AX7032a	5.38%	3.96%	26.39%
AX7028	5.34%	3.87%	27.53%
AX7035a	5.06%	3.40%	32.81%

Table 7: Mean value of the reflection of each sample from Length series

Full 3D electromagnetic modeling of light interaction with embedded NWs array was done by Nicklas Anttu to check the compatibility between the theoretical and experimental results. The modeling was done for both types of experiment and for InP NW array embedded into PDMS with square pattern 400 nm in pitch. An Average diameter of 136 nm was considered for the length series and a length average of 1520 nm was considered for the diameter series. The reflectance $R(\lambda)$ and transmittance $T(\lambda)$ were modeled and calculated when air-NW/PDMS interface is illuminated with light source as it is shown in figure 4.6(b). Afterwards, the absorption $A(\lambda)$ was calculated from $A(\lambda) = 1 - R(\lambda) - T(\lambda)$.

Figure 4.8 gives modeled and measured data for the length series, which show good agreement with each other. Modeled transmission through the NWs shows very good agreement but the measured reflection data is below modeled data with discrepancy about 0.02% due to roughness of the backside of membrane after peeling while it was modeled for the flat surface. The non-flat surface of the membrane was due to breaking point of the NWs was not at a same level as shown in figure 4.5(b). Such a roughening is expected to work as a partial anti-reflection interface/coating, decreasing the reflectance compared to that of a smooth interface [43]. SEM inspection was done on the backside of the membrane to check the flatness of the membrane as it is shown in figure 4.8(d).

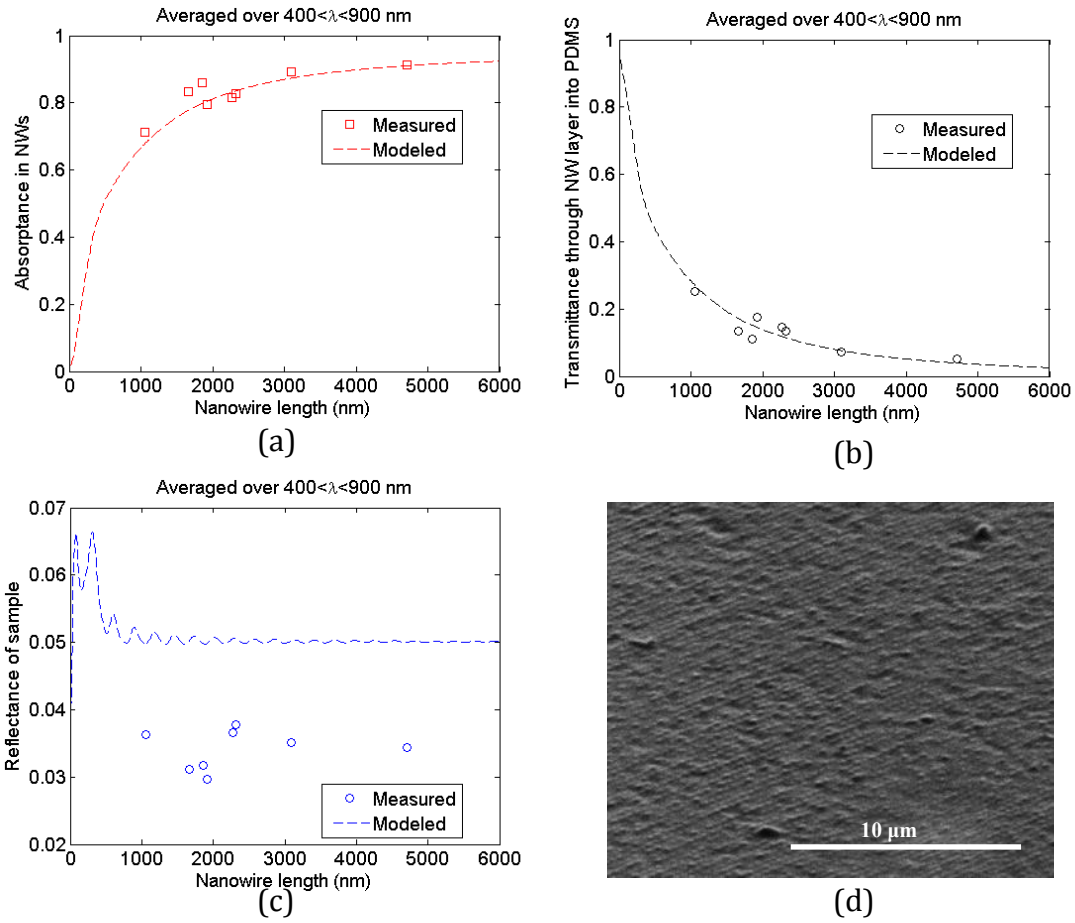

Figure 4.8: Measured and modeled wavelength-averaged absorption, reflection, and transmission of NW arrays as a function of NW length *L*. The average diameter of the fabricated samples lies in the range of *D* = 129 ± 3 nm to 147 ± 4 nm. The modeled NW arrays have NWs of diameter *D* = 136 nm, which is the mean of the average diameters of the fabricated samples.

In the same way, measurement and modeling was done for the diameter series with $L \approx 1600$ nm and varying diameter; tables 7, 8 and 9 show the measured data for absorption, transmission and reflection respectively. It was observed that the absorption increased rapidly by increasing diameter from the smallest experimental value of $D = 132 \pm 3$ nm with $A_{mean} = 70$ % to 92% for $D = 241 \pm 13$ nm. Even NWs with a length of $L < 2000$ nm can absorb light efficiently by optimizing the nanowire geometry. The sample with thicker NWs diameter D =347±34 nm also absorbed approximately same amount of incident light $A_{mean} = 93\%$.

Sample ID	Final Length (nm)	Diameter (nm)	Absorption Top up (%)	Absorption Top down (%)	Difference top up & down (%)
AX7039a	1560±26	132±3	68.58%	69.59%	1.45%
AX7037a	1470±41	157±6	74.46%	74.24%	0.30%
AX7036a	1608±87	181±11	81.74%	82.58%	1.02%
AX7038a	1553±86	241±13	91.34%	91.82%	0.52%
AX7040a	1520±70	347±34	91.58%	92.99%	1.52%

Table 8: Mean value of the absorption of each sample when top and bottom of the membrane is illumitated from dimater series.

Sample ID	Transmission Top Up (%)	Transmission Top Down (%)
AX7039a	24.25%	23.81%
AX7037a	16.59%	17.12%
AX7036a	9.72%	9.92%
AX7038a	2.83%	2.81%
AX7040a	1.40%	1.84%

Table 9: Mean value of the tranmission of each sample from dimater series

Sample ID	Reflection Top Up (%)	Reflection Top Down (%)
AX7039a	7.17%	6.60%
AX7037a	8.94%	8.64%
AX7036a	8.54%	7.50%
AX7038a	5.84%	5.37%
AX7040a	7.02%	5.17%

Table 10: Mean value of the reflection of each sample from dimater series

Figure 4.9 shows compatibility of the measured and modeled data for absorption, transmission and reflection. Generally the agreement between measured and modeled absorption for these diameter series is very good, see Figure 4.9(a). However, noticeable discrepancy between measured and modeled absorption was observed for the two largest diameters (D = 347 ± 34 nm, D = 241±13 nm). For the modeled spectra the absorption is drastically increased by increasing NWs diameter, but for diameter increase further than 200 nm the absorption starts decreasing. However, the measured data showed increase in absorption up to 93% for diameter larger than 200 nm.

This discrepancy can be traced to a difference between the measured and modeled reflectance. By increasing the diameter from 0 to 400, the modeled reflectance increases monotonously from 3 % to 24 % figure 4.9(c). In strong contrast, the measured reflectance showed diameter independent behavior with values of the order of 4 % for all the diameter series samples. As mentioned before, the diameter series samples have the two-diameter geometry, whereas the modeled NWs are of a constant

diameter along the NW length. The diameter for all of these samples is smaller and almost the same ($D \approx 135$ nm) at the bottom part of grown NWs. Such two-diameter NWs have been previously reported to strongly decrease the reflectance of NW arrays [44]. The independence of the reflection is possibly due to the similarity of the diameter at the bottom part, which was facing the light source at the experiment. The results demonstrate that by reducing the reflection losses, the range of NW diameters suitable for absorption applications can be extended considerably.

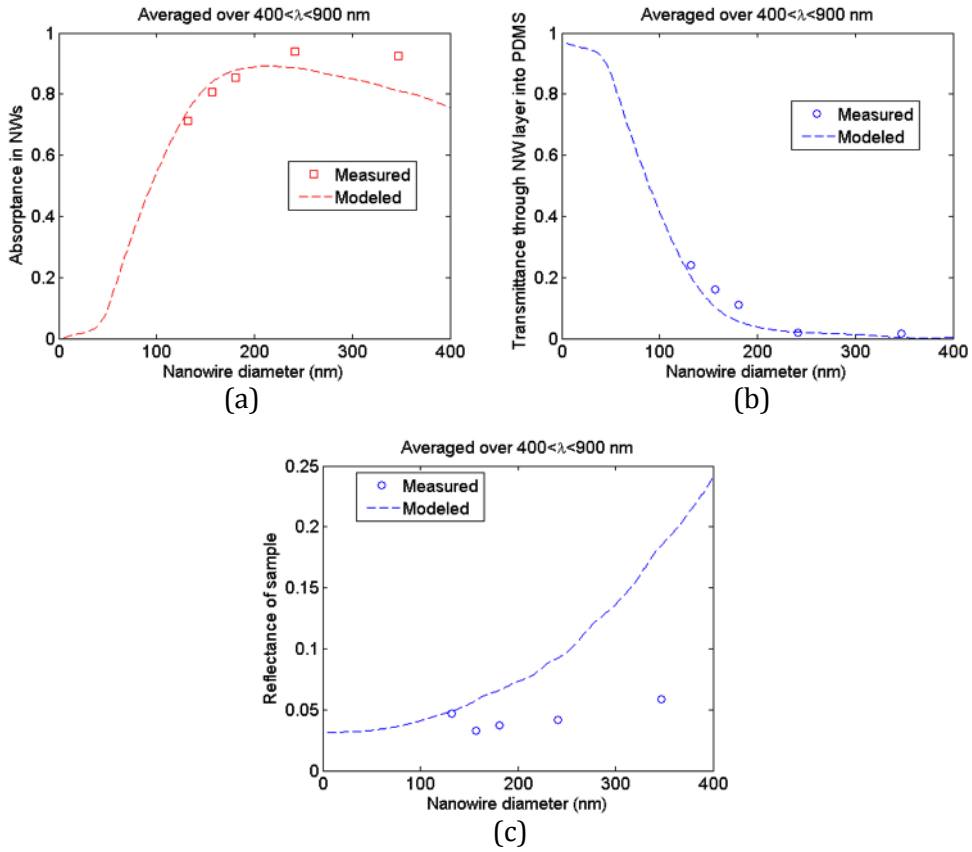

Figure 4.9: Measured and modeled wavelength-averaged absorption, reflection, and transmission of NW arrays as a function of NW diameter *D*. The average length of the NWs on the fabricated samples lies in the range of L = 1441 ± 70 nm to 1663 ± 86 nm. The modeled NW arrays have NWs of length L = 1570 nm, which is the mean of the average lengths of the fabricated samples.

4.3 Solar Cell Device

4.3.1 Introduction

The photons of sunlight incident to a semiconductor material will be reflected back, will be absorbed or will be transmitted trough the semiconductor. Reflected and transmitted photons are considered as losses in a photovoltaic device since only absorbed photons can generate power [45]. Absorbed photons can excite electrons from the valence band to the conduction band and generate electron-hole pairs in a band-to-band transition. Only photons with energy equal or more than the bandgap ($\geq E_g$) can be absorbed and photons with energy lower than the bandgap will be lost. Generally the photons with higher energy are absorbed more readily within short length of penetration trough the semiconductor due to higher absorption coefficient while photons with lower energy penetrate deeper before absorption. Based on absorption coefficient, different thickness of each semiconductor martials is required to absorb all of the non reflected incident photons (light); for instance for InP and GaAs, 1μm is a sufficient thickness, which for Si is 1000 times larger [31][46].

Generated electrons and holes may recombine since they are not in equilibrium. To reduce the probability of a recombination they must be spatially separated, otherwise they are considered as loss since they cannot be extracted. This can be done by the action of built-in electric field induced at the p-n junction. If the generated carriers can reach at the junction they will be swept across the junction; holes will be swept to the p-region and electrons to the n-region. This process is called carrier collection as it is illustrated in figure 4.10(a). But not all of the generated carriers can be collected. The collection probability mainly depends on the carrier diffusion length compared to the distance that they must travel to reach the junction (drift region w). By contacting to the both n- and p-regions and connecting them together, generated charge carrier (electrons and holes) can be extracted to the external circuit and generate net current, which is called light-generated current [31][45][46].

The generated current cannot generate power itself; voltage also must be generated in order to generate the electrical power. When the external circuit is open, n and p-region are not connected to each other, and the number of the electrons at n side and holes at p side will be increased by carrier collection since generated carries after separation cannot be extracted into an external circuit. The increase of charges creates an electric field opposite to the electric field induced by p-n junction, thus the net electric field will be decreased. It is similar to the p-n junction being forward biased, so the voltage will be created across the junction by this mechanism, which is called photovoltaic effect [31][45][46].

Solar cells are characterized by *I-V* measurement at dark and under illumination to observe the device performance and measure device parameters as it is shown in figure 4.10 (b). One of the key parameter of solar cells performance is the efficiency (η), which is defined as the ratio of electrical power produced by solar cell to incident power by sunlight. It is extracted by two main parameters, open-circuit voltage (V_{OC}) and short-circuit current (J_{SC}). The V_{OC} and J_{SC} are voltage at zero current flow and

current through the circuit whit no voltage across the device respectively. J_{SC} is the maximum of light-generated current and V_{OC} is the maximum voltage produced by solar cell and the power is zero at both of these points since one of the component either current or voltage is zero for each of these point. The filling factor (*FF*) is the ratio of maximum power produced by device to product of V_{OC} and J_{SC}. The maximum power point (*MPP*) as illustrated is the product of V_{MPP} and J_{MPP}. High performance solar cells have 0.80–0.89 in filling factor. The light-generated current and filling factor and efficiency of the solar cell are defined as below [31][45][46]:

$$J(V) = -J_{SC} + J_0(e^{qV/nkT} - 1)$$

$$FF = \frac{V_{MPP} I_{MPP}}{V_{OC} I_{SC}}$$

$$\eta = \frac{P_{max}}{P_{in}} = \frac{FF\, V_{OC} I_{SC}}{P_{in}}$$

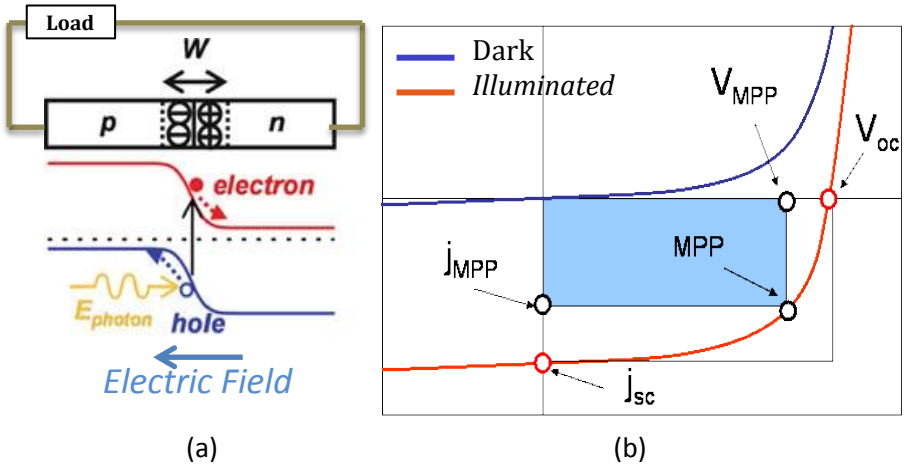

Figure 4.10: a) Band structure of p-n junction solar cell; an electron-hole pair is created by the photon absorption and separated by the built in electrics field. b) *I-V* of a solar cell device, current density under dark (blue) and illumination (red) vs. bias voltage. MPP indicates maximum power point, which is the maximum power provided by the cell.

4.3.2 Device Fabrication

InP NWs array with p-i-n axial junction and 2.5 µm in length and 190 nm and square pattern with 400 nm in pitches were used. InP was considered because of its low surface recombination velocity compared to GaAs and also ability of growth and doping of InP NW here at Lund NanoLab. First a thin layer of SiO_2 (approximately 10 nm) was deposited by Atomic Layer Deposition (ALD) technique to cover all around the NWs and then to reveal the tip of the NWs, SiO_2 was etched back by RIE. Then SolOne™ was applied to embed the NWs. After peeling the NWs with SolOne™, 25/250/25 nm of Ti/Au/Ti was deposited on the backside of the membrane

by sputtering. Since the polymer membrane is not heat resistant sputtering was done at low power and pressure to prevent swelling up of the membrane which have seen before for higher sputter power, due to heat during the sputtering process. 1-inch Si wafers were prepared by spinning PDMS 601 as a bonding matrix. Then the samples were placed from backside on top the PDMS. To cure the PDMS, the samples were placed on the oven at 80° C for 1 hour. Afterward, samples were left on Thinner (SolOne™ Dissolving Chemical) for 12 hours to dissolve the SolOne™ membrane. Then Samples were rinsed with IPA (Isopropanol) and dried by an N_2 gun.
Figure 4.11 shows the NWs array before and after transferring. Here it is really important to maintain the array structure of the NWs upon transfer.

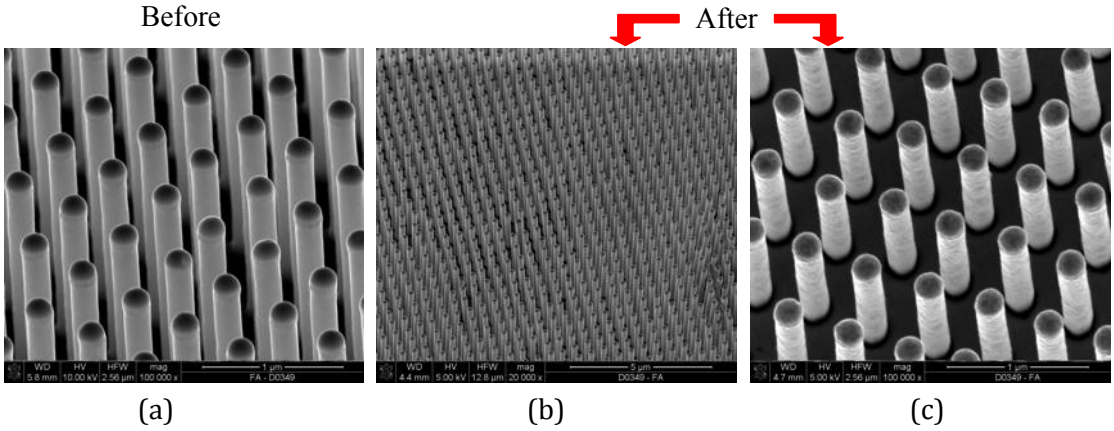

Figure 4.11: SEM images at 30° tilt before and after transferring a) NWs after growth with D = 190 nm, L = 2.5 µm, and P = 500 nm; a thin layer of SiO_2 was deposited and the tips of the NWs were revealed. b) Array of NWs peeled off and transferred to silicon substrate. c) Image with higher magnification after transferring, orientation of the NWs was maintained as grown which is really important for this transferring technique.

After NWs transferring, planarization was done for all of the samples by spinning Shipley 1813 (S1813) photoresist at 3000 rpm for 1 min. To soft-bake photoresist samples were placed on hotplate at 90°C for 1 min. Planarization was done in order to prevent short-circuit by filling the space between top and bottom contact and also to keep the orientation of the NWs during the further processing by filling the space between the NWs. To reveal the tip of NWs for top contact, the S1813 was thinned down by applying UVL flat exposure for 4 s followed by 40 s of development with MF319. To remove the residual Plasma Preen was used at 5 mbar for 1 min. Afterwards, SEM inspection was done to make sure the tip of the NWs was revealed as it is shown in figure 4.12(a). For chemical and physical stability of photoresist, samples were hard-baked at 200°C for 20 min, for which the temperature was ramped to the annealing temperature to avoid shrinkage or crack of the photoresist. Then 150 nm of ITO was deposited on all the samples by sputtering as a top contact. ITO was selectively etched away by HCl 1:1 for 1 min to define couples of individual devices with two different area patterns 0.01 and 0.000049 cm^2 in each sample. To define the bond pad double-layer photoresist was applied to take the advantage of undercut formation after exposure during developing for lift-off step. For the first layer, LOR 30B was used and spun at 4000 rpm for 1min and soft-baked at 165°C for 5 min with ramping up the temperature. For the second layer S1813 was used and spun at 4000

rpm for 1 min and then soft-baked at 90°C for 1 min. Each of the samples was exposed for 20 sec by UVL followed by 90 s development with MF 319 then the sputter machine again was used to deposit 25/250 nm of Ti/Au and then samples left on remover 1165 for a couple of hours for lift-off process. The final device is shown in figure 4.12(b).

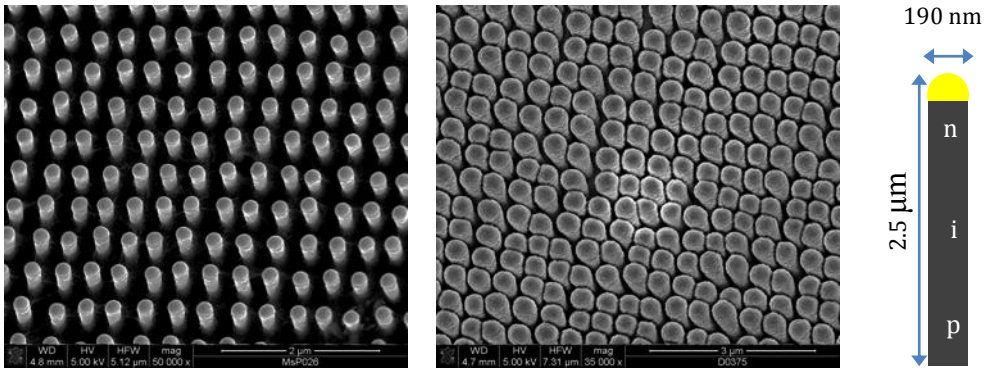

Figure 4.12: a) SEM images at 30° tilt after etching back the resist to expose the tip of the NWs for ITO deposition (front contact). b) SEM images at 30° tilt after ITO and Metal (Ti/Au) deposition. c) Schematic of the individual NW geometry.

Due to a mistake during processing the Ti/Au layer was deposited all over the ITO patterns. Also cracks, mostly on the bigger pattern, were observed caused during handling or processing of membrane. This leads to the top and bottom contacts being connected to each other, as shown in figure 4.13. Since no more samples were available sample at that time, it was not possible to do the whole device fabrication over again.

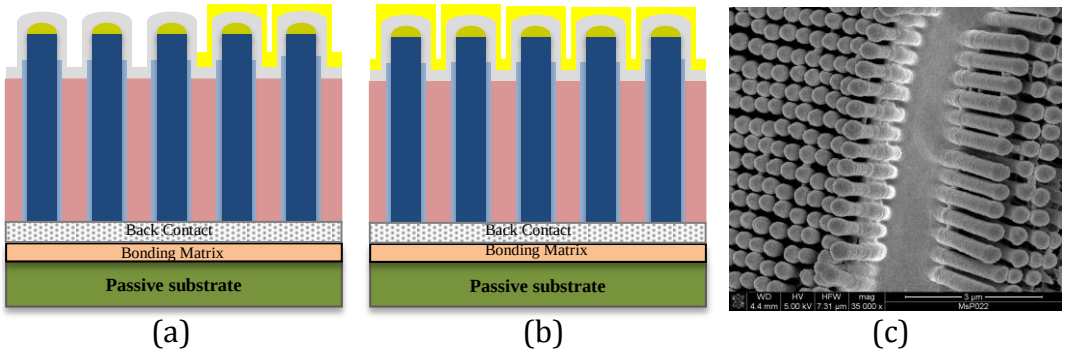

Figure 4.13: a) Schematic of designed device; the Au reposition designed to be at the edge of the cell to make it possible to go down with the probe without penetrating the cell. b) Schematic of fabricated device; due to a processing mistake, Ti/Au layer was deposited all over the device. c) SEM image of one fabricated cell; a crack was observed which makes the top and bottom contact connected due to resist missing between the cracks.

4.3.3 Measurement and Results

The standard characterization measurement for terrestrial solar cells is the use of a sun light simulator for air mass 1.5 spectrum, one-sun of illumination which is equal to 100 mW/cm^2 and 25 °C of cell temperature. The measurement set up is sketched in figure 4.14. The light was provided by sun simulator OREIL SOL 1 A and the samples were kept at adjusted height from the light source within 15 cm distance to keep the spectral constant. Two electrical probes were used to connect bottom and top contacts of the solar cell devices to a computer controlled current-voltage source KEITHLEY 2400-C. ORIEL Monocrystalline Silicon Solar Cell and its relevant Readout Meter were used for calibration by measuring the number of sun and device temperature. The whole setup was connected to the computer and controlled with software LabVIEW. First the current was measured by sweeping the voltage under dark (no illumination) and then the same measurement was done under illumination by opening the shutter of the sun simulator. All the important parameters of the device such as open-circuit voltage, short-circuit current, filling factor and efficiency were calculated instantly after measurement by software.

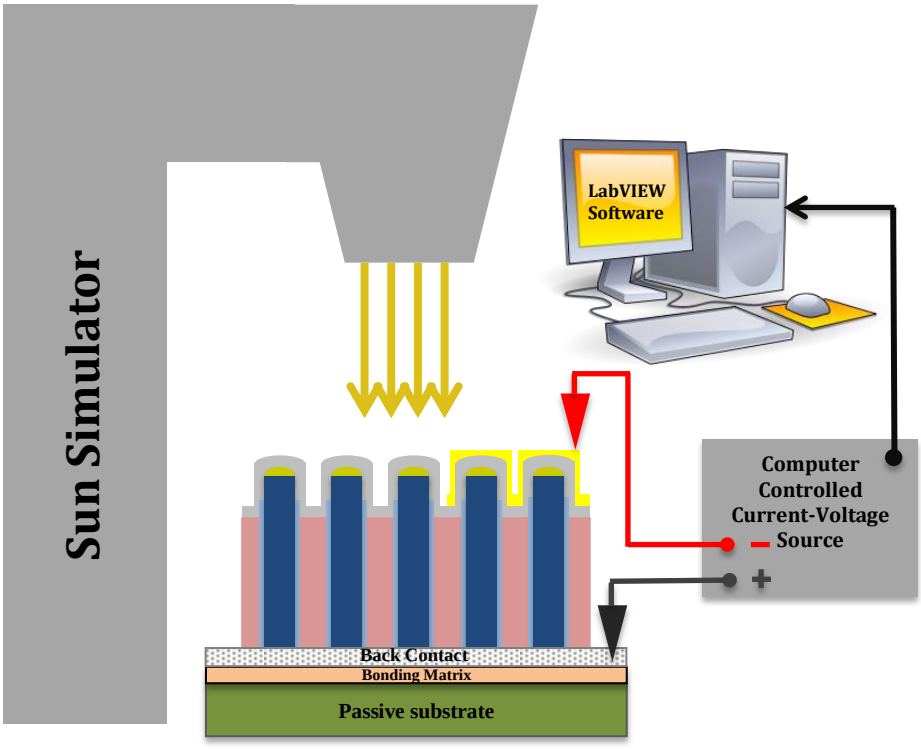

Figure 4.14: Schematic of simple solar cell *I-V* measurement; light is provided by the sun simulator with power of 100 mW/cm^2. Top and bottom contacts are connected to the current voltage source to sweep the bias voltage and measure the current. The whole set up is controlled by the pc with LabVIEW software.

Eighteen fabricated devices were measured. All the samples with 0.01 cm^2 area pattern showed short-circuit behavior probably due the crack shown in figure 4.13(c). Six of the smaller devices showed rectifying behavior with response to the light. The table 11 shows the measured device parameters. J_{SC} for all of them was really low due to the thin layer of Ti/Au deposited on top of the ITO all over the devices; subsequently most of the light was reflected back and was not absorbed by the NWs. The low V_{OC} is also due to the low light absorption since it is proportional to ln (I_L/I_0). The last two devices showed better performance in terms of J_{SC} and V_{OC}; more light absorption is one of the possibilities of the difference between devices. Since the four first devices were from another sample, the difference between lengths of the NWs tips reveled for top contact results in different thickness of the ITO and Ti/Au deposition. The difference of metal deposited thickness affects the light absorption through the NWs array. The *I-V* spectra for the device with highest efficiency is shown in figure 4.15 at both linear and logarithmic scales. The V_{oc} of 0.604 V and J_{SC} of 5.209 mA/cm^2 with filling factor of 16.74%, results in an efficiency of 0.527 % for the best device.

Devices	V_{OC} (V)	J_{SC} (mA/cm^2)	FF (%)	η (%)
1	0.340	0.376	24.94	0.032
2	0.330	0.399	25.65	0.034
3	0.389	0.436	23.79	0.040
4	0.347	0.559	20.18	0.039
5	0.609	4.720	16.43	0.472
6	0.604	5.209	16.74	0.527

Table 11:Comparison of the device performance by the main parameter of the solar cell

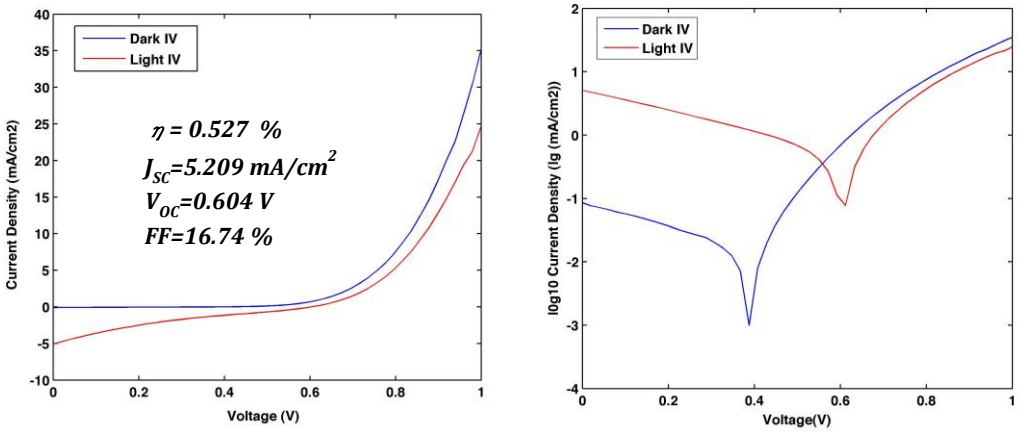

Figure 4.15: Linear (left) and logarithmic (right) spectra under dark (blue) and illumination (red) of the device with highest achieved efficiency.

Conclusions and Path Forward

The method of peeling off NWs from their native substrate by polymer and transferring them to the cheaper carrier substrate has been investigated and developed. Ordered arrays of NWs with length between 1.1-4.5 μm were successfully peeled off from their base and transferred with high yield of transformation while orientation of the NWs was preserved.

PL measurements on the membrane with embedded NWs showed that the fabricated NWs consisted of two different crystal structures zincblende and wurtzite.
Absorption through the ordered array of NWs without any contribution of substrate was investigated by measuring transmission and reflection through the membrane after peeling. The measurements demonstrate that the NWs can absorb all the incident light with energy above the band gap energy, which is coupled into the array, even if the NWs fill only a fraction of the volume of the NW array.
Solar cell devices were fabricated from transferred NWs and *I-V* measurements were done in order to observe the device performance. A V_{oc} of 0.604 V and J_{SC} of 5.209 mA/cm^2, was observed for the device with highest efficiency of 0.53 %, even though the top contact was not transparent in this case.

Further development is needed to face some of the challenges occurring during this work, such as finding peeling polymer with desirable characteristics for instance good enough strength to prevent breaking during peeling and also low viscosity that allows the polymer penetrate between the NWs all the way down to the bottom of the NWs. Since the processing of the embedded NWs without passive substrate is not possible at the moment (it is too thin and fragile) the bonding matrix is needed. If the peeling polymer is easy to remove some of the main problem with bonding matrix will be solved since some of the materials that have been tried as bonding matrix in this work were dissolving by the relevant membrane dissolver. The membrane also needs to be thin otherwise RIE etching is not possible due to Lund Nano Lab rules and restrictions.
Finding the compatible bonding matrix that can handle chemicals and the temperature of device processing is another challenge for this work. Also the way of handling the membrane during the work to decrease the possibility of introducing cracks needs to be further developed. The way of forming Ohmic contact to the NWs is another challenge, which has not been investigated in this work. Since annealing is the common method for Ohmic contact, temperature stability of the polymers is a further challenge to the ongoing project.

References

[1] E. b. R. Waser, Nanotechnology, vol. Volume3: Information Technology, John Wileys & Sons,(2008).

[2] K. V. Vijay, L. Chen och J. Xie, Nanomedicine: Design and Applications of Magnetic Nanomaterials, Nanosensors and Nanosystems, John Wileys & Sons, (2008).

[3] Kästner, G. & Gösele, U. Stress and dislocations at cross-sectional heterojunctions in a cylindrical nanowire. Philosophical Magazine **84**, 3803-3824, doi:10.1080/14786430420002813 89 (2004).

[4] C Patrik T Svensson, Thomas M˚artensson, Johanna Tra¨g˚ardh, Christina Larsson, Michael Rask, Dan Hessman, Lars Samuelson, Jonas Ohls- son, Monolithic GaAs/InGaP nanowire light emitting diodes on silicone, Nanotechnology 19, 305201 (2008).

[5] G. Kästner och U. Gösele, Philosophical Magazine, vol. 84, nr 3803, (2004).

[6] Fan HJ, Werner P, Zacharias M. Semiconductor nanowires: from self-organization to patterned growth. Small 2(6):700–17, (2006).

[7] Wacaser BA, Dick KA, Johansson J, Borgström MT, Deppert K, Samuelson L. Preferential interface nucleation: an expansion of the VLS growth mechanism for nanowires. Adv. Mater. 21(2), (2009).

[8] Fan Z, Razavi H, Do J, Moriwaki A, Ergen O, et al. Three-dimensional nanopillar-array photovoltaics on low-cost and flexible substrates. Nature Mater. 8(8), (2009).

[9] Central Intelligence Agency, 2009 The World Factbook. (CIA, 2009).

[10] International Energy Agency, 2013 Key World Energy Statistics. (IEA, 2013).

[11] International Energy Agency, 2013 CO2 Emission From Fuel Combustion Highlights. (IEA, 2011).

[12] Renewable Energy Policy Network for the 21st Century, Renewable 2013: Global Status Repot (REN21, 2013).

[13] U.S. Depatment of Energy. Basic Research Needs for Solar Energy Utilization. Argonne National Laboratory, (2005).

[14] Gregory Phipps, C. M. A. T. G. Renewable Energy Focus. Volume 9, Issue 4, (2008).

[15] Augustin Mcevoy, T. M. A. L. C. Practical handbook of photovoltaics: fundamentals and application. 2nd. ed. Elsevier, (2013).

[16] F. Dimroth. High-efficiency solar cells from III-V compound semiconductors. phys. stat. sol. (c) **3**, No. 3, 373–379 (2006).

[17] William Shockley and Hans J. Queisser. Detailed Balance Limit of Efficiency of p‐n Junction Solar Cells. Journal of Applied Physics, Volume 32, 1961.

[18] Muskens, O. L., Rivas, J. G., Algra, R. E., Bakkers, E. P. A. M. & Lagendijk, A. Design of Light Scattering in Nanowire Materials for Photovoltaic Applications. Nano Letters **8**, 2638-2642, doi:10.1021/nl0808076 (2008).

[19] Hu, L. & Chen, G. Analysis of optical absorption in silicon nanowire arrays for photovoltaic applications. Nano Letters **7**, 3249-3252, doi:10.1021/nl071018b (2007).

[20] M. T. Borgström, J. Wallentin, M. Heurlin, S. Fält, P. Wickert, J. Leene, M. H. Magnusson, K. Deppert, L. Samuelson, Nanowires With Promise for Photovoltaics. IEEE Journal of Selected Topics in Quantum Electronics, (2011).

[21] Erik C. Garnett, Mark L. Brongersma, Yi Cui, and Michael D. McGehee. Nanowire Solar Cells. Annu. Rev. Mater. Res. 2011.41:269-295.

[22] Gyu-Chul Yi. Semiconductor Nanostructures for Optoelectronic Devices. Springer-Verlag Berlin Heidelberg 2012.

[23] T. Fukui, M. Yoshimura, E. Nakai, and K. Tomioka. Position-Controlled III–V Compound Semiconductor Nanowire Solar Cells by Selective-Area Metal–Organic Vapor Phase Epitaxy AMBIO 41 (2012),119.

[24] Wallentin, J. et al. InP Nanowire Array Solar Cells Achieving 13.8% Efficiency by Exceeding the Ray Optics Limit. Science **339**, 1057-1060, doi:10.1126/science.1230969 (2013).

[25] A J Standing, S Assali, J E M Haverkort and E P A M Bakkers. High yield transfer of ordered nanowire arrays into transparent flexible polymer films. IOP Nano 23, 495305, (2012).

[26] Plass K E, Filler M A, Spurgeon J M, Kayes B M, Maldonado S, Brunschwig B S, Atwater H A and Lewis N S. Flexible Polymer-Embedded Si Wire Arrays. Adv. Mater. 21 325–8 (2009).

[27] Piruska, A.; Nikcevic, I.; Lee, S. H.; Ahn, C.; Heineman, W. R.; Limbach, P. A.; Seliskar, C. J. Lab Chip, 5, 1348-54, (2005).

[28] From James M. Spotts 2008 Microfluidics Course Institute for Systems Biology November 17, (2008).

[29] Characterization of Polydimethylsiloxane (PDMS) Properties for Biomedical Micro/Nanosystems, Biomedical Microdevices 7:4, 281–293, (2005).

[30] F. Léonard and A. Alec Talin. Electrical contacts to one- and two-dimensional nanomaterials. Nature, DOI: 10.1038/NNANO (2011).

[31] S.M. Sze, Kwok K. Ng. Physics of Semiconductor Devices. John Wiley & Sons, Inc (2007).

[32] S. Hwang, J. Shim, and Y. Eo. Ohmic Contacts of Pd/Zn/Pt(or Pd)/Au Materials to P-type InP. IEEE (2005).

[33] WILKINSON, A. D. M. A. A. Compendium of Chemical Terminology. 2nd. ed. IUPAC, (1977).

[34] KIRA, M.; KOCH, S. W. Semiconductor Quantum Optics. Cambridge University Press, 2011.

[35] Hass G. Filmed surfaces for reflecting optics. J. Opt. Soc. Am. 45: 945-52, (1955).

[36] Hobbs, Douglas S., Bruce D. MacLeod & Juanita R. Riccobono. "Update on the Development of High Performance Anti-Reflecting Surface Relief Micro-Structures." SPIE 6545-34, (2007).

[37] Yablonovich E, Cody GD. Intensity Enhancement in Textured Optical Sheets for Solar Cells. IEEE Transactions on Electron Devices. 1982 ;ED-29:300-305.

[38] Anttu, N. Geometrical optics, electrostatics, and nanophotonic resonances in absorbing nanowire arrays. Opt. Lett. **38**, 730-732 (2013).

[39] Anttu, N. & Xu, H. Q. Coupling of Light into Nanowire Arrays and Subsequent Absorption. Journal of Nanoscience and Nanotechnology **10**, 7183-7187, doi:10.1166/jnn.2010.2907 (2010).

[40] Anttu, N. & Xu, H. Q. Efficient light management in vertical nanowire arrays for photovoltaics. Opt. Express **21**, A558-A575 (2013).

[41] Huang, N., Lin, C. & Povinelli, M. L. Broadband absorption of semiconductor nanowire arrays for photovoltaic applications. Journal of Optics **14**, 024004 (2012).

[42] Hu, L. & Chen, G. Analysis of optical absorption in silicon nanowire arrays for photovoltaic applications. Nano Letters **7**, 3249-3252, doi:10.1021/nl071018b (2007).

[43] Chattopadhyay, S. et al. Anti-reflecting and photonic nanostructures. Materials Science and Engineering: R: Reports **69**, 1-35, doi:http://dx.doi.org/10.1016/j.mser.2010.04.001 (2010).

[44] Fan, Z. et al. Ordered Arrays of Dual-Diameter Nanopillars for Maximized Optical Absorption. Nano Letters **10**, 3823-3827, doi:10.1021/nl1010788 (2010).

[45] Jenny Nelson: The Physics of Solar Cells. Imperial College Press, (2003).

Peter Wurfel: Physics of Solar Cells: From Principle to New Concepts Wiley-WHC,Weinheim, (2005)

Publication

Nano Res
DOI: 10.1007/s12274-014-0441-z
Research Article

Absorption of light in InP nanowire arrays

Nicklas Anttu[1,*](✉), Alireza Abrand[1,2,*], Damir Asoli[2], Magnus Heurlin[1], Ingvar Åberg[2], Lars Samuelson[1], and Magnus Borgström[1]

[1]Division of Solid State Physics and The Nanometer Structure Consortium at Lund University (nmC@LU), Lund University, Box 118, 22100 Lund, Sweden.
[2]Sol Voltaics AB, Ideon Science Park, Scheelevägen 17, 22370 Lund, Sweden.

*These authors contributed equally
†Email: nicklas.anttu@ftf.lth.se

Received: day month year / Revised: day month year / Accepted: day month year (automatically inserted by the publisher)

ABSTRACT

An understanding of the absorption of light is essential for efficient photovoltaic and photodetection applications with III-V nanowire arrays. Here, we correlate experiments with modeling and verify experimentally the predicted absorption of light in InP nanowire arrays for varying nanowire diameter and length. We find that 2000 nm long nanowires in a pitch of 400 nm can absorb 94 % of the incident light with energy above the band gap, a consequence of that light which in a simple ray-optics description would be travelling between the nanowires can be efficiently absorbed by the nanowires. Our measurements demonstrate that the absorption for long nanowires is limited by insertion reflection losses when light is coupled from the air top-region into the array. These reflection losses can be reduced by introducing a smaller diameter to the nanowire-part closest to the air top-region. For nanowire arrays with such a nanowire morphology modulation, we find that the absorptance increases monotonously with increasing diameter of the rest of the nanowire.

KEYWORDS

Indium phosphide, semiconductor, nanowire, absorption of light

1. Introduction

Vertical III-V nanowire (NW) arrays have gained considerable recent interest for photovoltaics[1-4] and photodetectors [5,6]. The NW geometry has distinct material science benefits compared to the conventional thin-film geometry. For example, the free surface of the NWs allows for efficient defect-free strain relaxation as compared to thin-films of the same materials [7-10], thus opening a large pallet of lattice-mismatched material combinations for tailoring the properties of opto-electronic devices. Furthermore, NWs of the opto-electronically highly interesting but expensive III-V materials can be fabricated on a lattice mismatched substrate of a much cheaper material, such as silicon [11].

Semiconductor NW arrays can interact strongly with light [12-14], and the interest of using NW arrays for photovoltaics and photodetection is founded to a large extent on theoretical predictions [13,15-20] that NW arrays due to their geometry

Address correspondence to Nicklas Anttu, nicklas.anttu@ftf.lth.se

can absorb light efficiently. Indeed, it was recently demonstrated that an InP NW array with an axial pn-junction could convert more than 70 % of the photons of the solar spectrum with energy above the band gap of InP into photocurrent, giving rise to a record 13.8 % conversion efficiency in a cell of 1 mm² in area [1]. However, a systematic experimental study of the absorption of light in III-V NW arrays has not been performed. By increasing our understanding of the interaction between light and nanowires, such a fundamental study holds the prospect of leading to optimization of the materials and enhanced performance in nanowire-based opto-electronics.

Here, we study experimentally the absorption of light in InP NW arrays for varying NW diameter and NW length. The epitaxially fabricated NW arrays were embedded in polydimethylsiloxane (PDMS) matrices and peeled off from the native, opaque growth substrate. Next, we performed transmission and reflection measurements in the visible and the near-infrared wavelength region where the PDMS is transparent. From these measurements, the absorption of light in the NWs could be determined. We found that a NW length of 2000 nm is sufficient for absorbing more than 94 % of the incident light averaged over the wavelength range from 400 nm to 900 nm. Indeed, our measurements demonstrate that a NW array can absorb all incident light with energy above the band gap, limited only by the insertion reflection losses when light is coupled from the air top-region into the array. We found that these reflection losses are reduced in a NW geometry where the NW-part closest to the air top-region shows a smaller diameter than the rest of the NW.

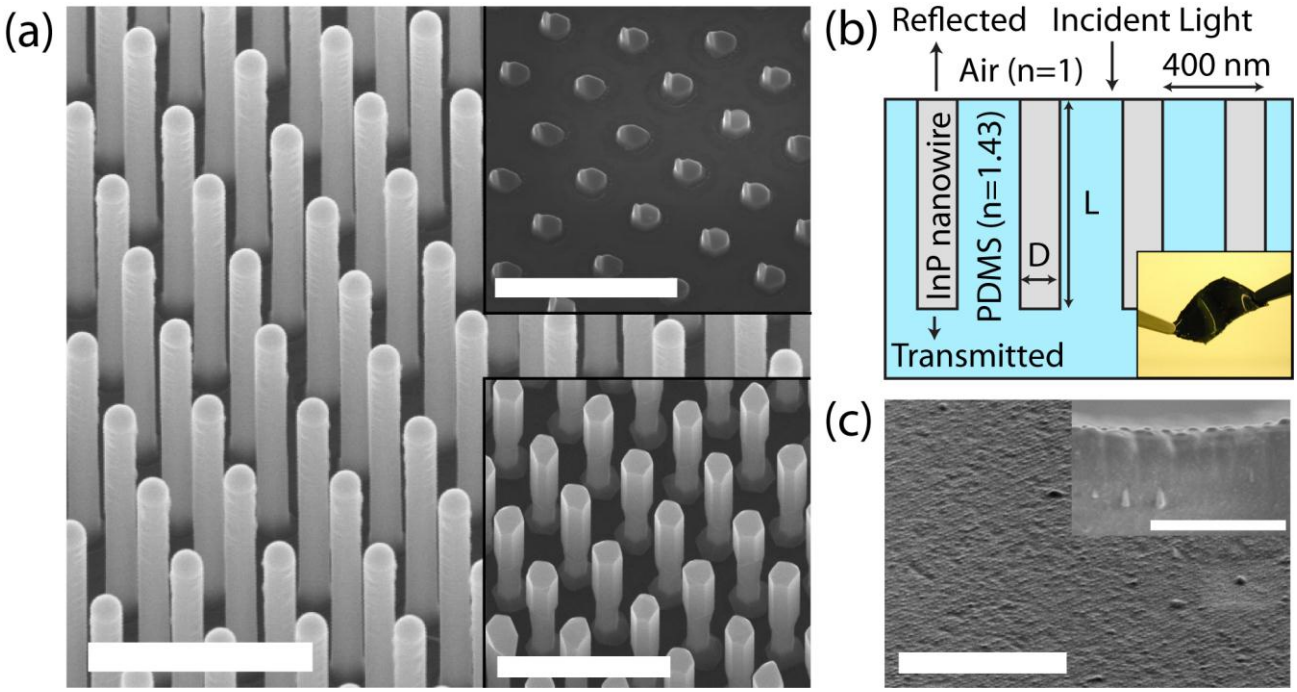

Figure 1: a) SEM image at 30° angle from top view of a fabricated InP NW array with period p = 400 nm and NWs of diameter D = 138 ± 4 nm and length L = 1620 ± 40 nm. Top inset: SEM image of the substrate of the same sample after peeling of the NWs. Notice how the NWs were ripped off nicely at their base. Bottom inset: SEM image at 14° angle of fabricated NWs of L = 1653 ± 87 nm showing a dual-diameter geometry with a diameter of D = 181 ± 11 nm at the top of the NWs and a diameter of D = 133 ± 3 nm at the bottom. All the scale-bars are 1 μm here. b) Schematic view of InP NWs embedded in PDMS. Notice that after the peel-off, the bottom of the as-grown NWs is located at the top air-NW/PDMS interface. Inset: Photograph of one of the PDMS membranes after peel-off. c) SEM image at 50° angle of the air-NW/PDMS interface of one the membranes. The scale-bar is 10 μm. Note the roughened air-NW/PDMS interface after peel-off. Inset: SEM image at 10° tilt of the cross-section of one of the membranes after cleaving the membrane. The scale bar is 3 μm.

Furthermore, in such a nanowire morphology, the absorptance increases monotonously with increasing

Address correspondence to Nicklas Anttu, nicklas.anttu@ftf.lth.se

diameter of the rest of the NW. This makes it feasible to tune the NW geometry in order to increase the absorptance even more efficiently with respect to materials consumption than for the case of straight, cylindrical InP NWs, for which a diameter of approximately 200 nm in a pitch of approximately 500 nm has been predicted to yield a high absorptance [17,18].

2. Experimental

For the experimental investigations, two series of NW arrays were fabricated with either different NW length or different NW diameter. The dimensions of the NWs in the peeled-off PDMS membranes were determined from scanning electron microscope (SEM) images as follows. The average diameter D and the corresponding standard deviation was determined by measuring the diameter at the top of 50 as-grown NWs (Figure 1a) for each sample. For the NW length L, the average length $L_{as\text{-}grown}$ and its standard deviation $s_{as\text{-}grown}$ of the same 50 as-grown NWs was measured first. Next, the average length L_{stub} and its standard deviation s_{stub} of 50 stubs left on the substrate after peel-off was measured (top inset in Figure 1a). Then, the NW length L in the PDMS membrane was calculated as $L = L_{as\text{-}grown} - L_{stub}$ with standard deviation given by $s = [s_{as\text{-}grown}^2 + s_{stub2}]^{(1/2)}$. In the quoted values, the uncertainty denotes the standard deviation in length and diameter, respectively.

The first growth series consisted of eight samples of NW arrays grown for different times. Since the growth time is related to the nanowire length, this allowed us to investigate the dependence between the nanowire length and the absorption of light. The average length ranged from L = 955 ± 35 nm to L = 4492 ± 96 nm. For this series, the average NW diameter varied slightly, from D = 129 ± 3 nm to D = 147 ± 4 nm. To allow for an investigation of the effect of the NW diameter on the absorption, the second growth series consisted of five NW arrays with average diameter varying from D = 132±3 nm to D = 347±34 nm. For this series, the average NW length varied slightly, from L = 1441 ± 70 nm to L = 1663 ± 86 nm.

In more detail, samples were prepared for NW growth by defining 160 nm diameter and 20 nm high Au catalyst particles in periodic arrays with a period of 400 nm using nanoimprint lithography on InP (111)B substrates. Notice that this period is predicted to yield a high absorptance in the nanowires if the nanowire diameter is chosen suitably [17,18] For the second growth series where the diameter was varied, an additional 20 nm thick SiN_x layer was used as a growth mask between the Au particles. The NWs were grown in a low-pressure (100 mbar) metal organic vapor phase epitaxy (MOVPE) system (Aixtron 200/4) with a total flow of 13 l/min using hydrogen (H_2) as carrier gas. For InP growth, trimethylindium (TMI) and phosphine (PH_3) were used as precursors, with constant molar fractions of $\chi_{PH3} = 6.9\times10^{-3}$ and $\chi_{TMI} = 74.3\times10^{-6}$, except for the longest NWs that had an average length of L = 4492 ± 96 nm for which $\chi_{TMI} = 100.4\times10^{-6}$ was used. Hydrogen chloride (HCl) was used to control the radial growth19 at a molar fraction of $\chi_{HCl} = 6.2\times10^{-5}$. The samples were first annealed at 550 °C for 10 min under a PH_3/H_2 gas mixture to desorb any surface oxides. The reactor was then cooled to 440 °C, at which growth was initiated by adding TMI to the flow. After a 15 s nucleation time where $\chi_{PH3} = 2.1\times10^{-3}$, HCl was added and nominally intrinsic InP NWs were grown. For the length series, eight samples were grown for different times varying between 5 and 25 min. For the diameter series consisting of five samples, the core NWs were grown for 14 min. For both series, growth was terminated by switching off the TMI flow, and the sample was cooled down in a PH_3/H_2 gas mixture. For the diameter series, the Au particles were removed by wet chemical etching in a $KI:H_2O:I_2$ solution after which the NW cores were reinserted into the growth chamber for shell growth at a temperature of 575 °C in order to increase the diameter of the NWs. For this growth step $\chi_{TMI} = 65.4\times10^{-6}$ and $\chi_{PH3} = 11.5\times10^{-3}$. Here, the growth time was varied from 1.5 to 20 min.

For the spin-on of PDMS, all the samples were bonded to 1-inch silicon substrates by crystal bonding. Wacker 625A PDMS and its curing agent 625B were used. After mixing with a weight ratio of 9:1, droplets of the mixture were dropped on the samples. The mixture was allowed to penetrate and fill out the space between the NWs for 2 min. Next, the samples were spun at a spin-coating speed of 800 rpm for 35 sec to obtain an even film of PDMS. All the samples were placed in an oven at 80° C for 1

Address correspondence to Nicklas Anttu, nicklas.anttu@ftf.lth.se

hour to cure the PDMS. Afterwards, the PDMS membranes containing the NWs were peeled off with tweezers (see inset in Figure 1b). We note that the NWs kept their orientation with respect to each other also in the PDMS matrix after the peel-off (see inset in Figure 1c).

To measure the total absorptance $A(\lambda)$ of the embedded NWs, total reflectance $R(\lambda)$ and total transmittance $T(\lambda)$ were measured separately. The absorptance of the NWs was then obtained as $A(\lambda) = 1- R(\lambda) - T(\lambda)$. In the measurements, the air-NW/PDMS interface of each sample was irradiated by a white-light source (AvaLight-HAL), and in each measurement either reflected or transmitted light was collected by an integrating sphere (AvaSphere-30-REFL) and analyzed with a spectrometer (AvaSpec-ULS3648). The measurements were performed in the wavelength range of $400 < \lambda < 900$ nm[a] with a wavelength step of $\Delta\lambda = 0.35$ nm using a 15×10^3 ms integration time both for the reflectance and the transmittance measurements. A spot of approximately $1\times\pi$ mm^2 in area was irradiated in both types of measurements.

For the reflectance measurements, light was sent through the entrance view-port into the sphere and toward the sample view-port and the underlying sample. The light that was transmitted through the sample was allowed to pass to the exterior of the sphere without additional reflections back into the sphere. Here, the calibration and normalization was performed by using a planar silicon substrate sample as a reference. The background was calibrated for by measuring the stray light inside the sphere when no sample was attached to the sample view-port. For the transmittance measurements, light was instead sent into the sphere through the sample and the sample view-port. Here, the reference level was measured when no sample was mounted, and the background level was measured with the light source turned off. For both the reflectance and the transmittance measurements, the incidence angle was approximately 8° from the normal incidence that maximizes the area of the nanowire array to the incident light.

To support the experimental findings, we have performed full three-dimensional electromagnetic modeling [21] of the interaction of light with the NW arrays. In this modeling, we consider normally incident light since the 8° incidence angle in the experiments is expected to have only a minor effect on the results [16]. The modeled NW array consists of InP NWs placed in a square pattern of period p = 400 nm into a PDMS matrix with air on the top side (Figure 1b). The NWs in the modeling are of length L and have a circular cross-section of diameter D. For the InP, tabulated values for the refractive index $n(\lambda)$ were used [22], and for the PDMS a wavelength independent value of n = 1.43 was used. In the modeling, the reflectance $R(\lambda)$ of the sample and the transmittance $T(\lambda)$ into the PDMS below the NWs were calculated. Afterwards, the absorptance $A(\lambda)$ was calculated from $A(\lambda) = 1- R(\lambda) - T(\lambda)$.

1. Results and discussion

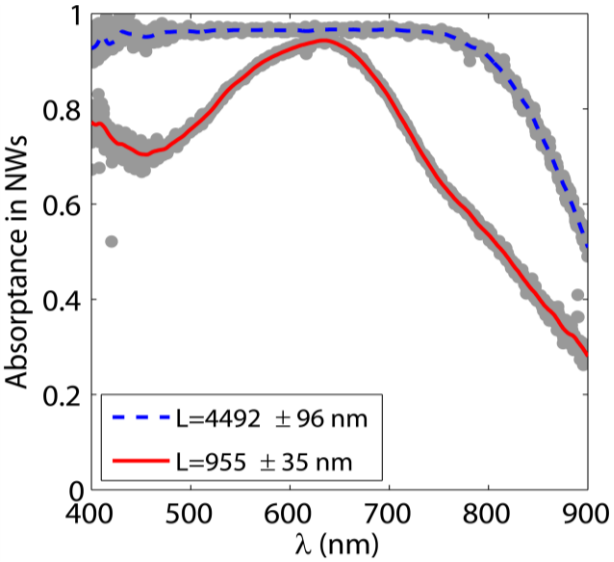

Figure 2. Measured absorptance of two InP NW arrays of similar NW diameter of D = 132 ± 10 nm (solid line) and 147 ± 4 nm (dashed line) but considerably varying NW length of L = 955 ± 35 nm (solid line) and 4492 ± 96 nm (dashed line). The gray circles indicate the measured values and the lines are calculated from these values as a moving average over 20 nm in wavelength.

A study of the spectrally resolved absorptance $A(\lambda)$ for varying NW length L can reveal many important

[a] This wavelength range is defined by a high signal to noise ratio in the measurements. Coincidentally, the upper limit of this range matches nicely the band gap of InP which is 925 nm in wavelength.

Address correspondence to Nicklas Anttu, nicklas.anttu@ftf.lth.se

details about the optical response of NW arrays (Figure 2). For this purpose, we concentrated on two NW arrays with NW diameter $D \approx 140$ nm. With this choice for the diameter, the NWs fill just 10 % of the volume in the NW array, and the remaining 90 % is filled by the non-absorbing PDMS. The first array has NWs with $L = 955 \pm 35$ nm whereas the second array has considerably longer NWs with $L = 4492 \pm 96$ nm.

First, we find for the shorter NWs an absorptance peak of $A \approx 94$ % at $\lambda \approx 630$ nm. This absorptance peak in the measurements is attributed to the (diameter-dependent) resonant absorption predicted theoretically [15-17,23,24] and shown indirectly by photoconductivity measurements [6]. When moving toward shorter wavelengths from the absorptance peak, the absorptance dips to $A \approx 70$ % at $\lambda \approx 450$ nm after which it rises to $A \approx 80$ % at $\lambda = 400$ nm. In contrast, the absorptance decreases monotonously when moving toward longer wavelengths from the absorptance peak. Thus, for these short NWs, the absorptance shows a complicated and non-monotonous dependence with wavelength.

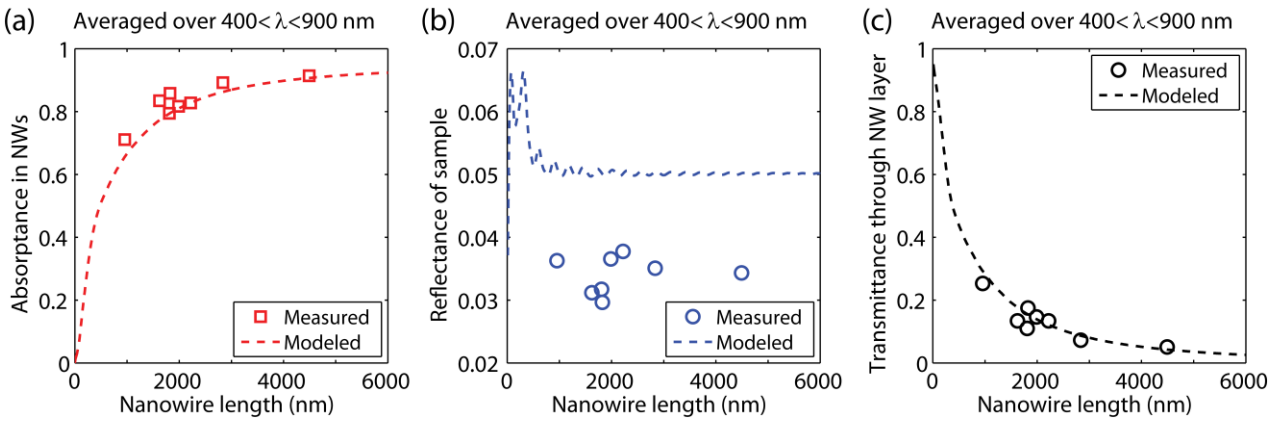

Figure 3. Measured and modeled wavelength-averaged absorptance, reflectance, and transmittance of NW arrays as a function of NW length L. The average diameter of the fabricated samples lies in the range of $D = 129 \pm 3$ nm to 147 ± 4 nm. The modeled NW arrays have NWs of diameter $D = 136$ nm, which is the mean of the average diameters of the fabricated samples.

In contrast, when considering the longer NWs with $L = 4492 \pm 96$ nm, the absorptance has saturated at a value of approximately 97 % for $\lambda < 700$ nm. Further analysis of the measured spectra revealed that the absorptance is limited by a spectrally independent reflection loss of 3 %, which we attribute to reflection at the air-NW/PDMS top interface. Furthermore, for these longer NWs, due to the saturation of the absorptance, the resonant absorption is not visible any longer at $\lambda \approx 630$ nm as was the case for the shorter NWs. Instead, the absorptance spectrum is now very similar to that expected for a homogenous thin film where the overall absorption is limited by reflection losses as well as the weak absorption coefficient close to the band gap. Thus, we find here direct evidence that a NW array can absorb all the incident light with energy above the band gap which is coupled into the array, even if the NWs fill only 10 % of the volume.

To systematically investigate the effect of the NW length on the absorptance, we turn to study all the eight fabricated arrays of $D \approx 140$ nm and varied length. For compact presentation of the results, we employ A_{mean}, the average of $A(\lambda)$ over the measurement range of $400 < \lambda < 900$ nm (Figure 3a). First, we find a rapid increase from $A_{mean} \approx 70$ % to $A_{mean} \approx 85$ % when the NW length is increased from the smallest fabricated value of $L \approx 1000$ nm to $L \approx 2000$ nm. However, the increase is less rapid for $L > 2000$ nm, and a further increase of the NW length to 4500 nm increases A_{mean} by just 0.06 to 91 %. This can be understood from the saturation of the absorptance with increasing length of the NWs (Figure 2). For long NWs, it is the absorptance for wavelengths close to the bandgap wavelength, which is 925 nm

Address correspondence to Nicklas Anttu, nicklas.anttu@ftf.lth.se

for InP, that increases with increasing length. This increase has only a minor effect on the wavelength averaged absorptance shown in Figure 3a. When these measured absorptance values are compared to the modeled values, we find excellent agreement (Figure 3a). The modeling shows a saturation toward the limiting value of A_{mean} = 95 % when $L \rightarrow \infty$ for a diameter of 140 nm.

To allow for a more detailed study of the absorption of light in the NW arrays, we show in Figure 3b and Figure 3c the measured and modeled wavelength-averaged reflectance and transmittance of the NW arrays. First, from the modeling, we expect for L > 1000 nm a reflectance of 5 %.[b] The measurements show however noticeably lower reflectance values on the order of 3.5 %. A possible explanation for this discrepancy between modeled and measured reflectance could be the slight roughening of the air-NW/PDMS interface during the peel-off from the native substrate (see Figure 1c). Such a roughening is expected to work as a partial anti-reflection interface/coating, decreasing the reflectance compared to that of a smooth interface [25]. When turning to the measured and modeled transmittance through the NW layer, we find excellent agreement (Figure 3c). At L = 2000 nm, the transmittance is less than 15 %, and at 4500 nm, the transmittance is less than 5 %. Thus, for these NWs with $D \approx$ 140 nm it is noticeably beneficial to increase the NW length beyond 2000 nm to enhance the absorptance.

Theoretically it has been predicted that the absorptance is strongly diameter dependent [1,6,15-18,23,24]. Indeed, by studying the five samples with $L \approx$ 1600 nm and varying D, we find that the absorptance increases rapidly when the diameter is increased from the smallest experimental value of D = 132 ± 3 nm (Figure 4a). For D = 241 ± 13 nm, the absorptance has increased to a high value of A_{mean} = 94 %. Thus, also NWs with a length of L < 2000 nm can absorb light efficiently by optimizing the nanowire geometry. We note that the agreement between measured and modeled absorptance is very good in general for these arrays (Figure 4a). However, for the largest fabricated diameter of D = 347 ± 34 nm, the measured absorptance is 93 % whereas the modeled absorptance is only 81 %. This discrepancy can be traced to a difference between the measured and modeled reflectance as described below.

The modeled reflectance increases monotonously from 3 % to 24 % when D increases from 0 to 400 nm (Figure 4b). In strong contrast, the measured reflectance is seemingly diameter independent and shows values on the order of 4 % for the fabricated NW arrays. Note that the modeled NWs are of a constant diameter along the NW length (see Figure 1b) whereas the fabricated NWs in this diameter-variation series show a two-diameter geometry (see bottom inset of Figure 1a). The diameter of these fabricated NWs is smaller close to the air-NW/PDMS top interface than further down in the PDMS layer, that is, the diameter of the as-grown NWs is larger at the top part of the NWs (see Figure 1b). Such two-diameter NWs have been previously reported to strongly decrease the reflectance of NW arrays [26,27]. We note that the diameter is approximately 140 nm at the air-NW/PDMS interface for all samples in this diameter-variation series, possibly explaining the independence of the reflectance on the quoted diameter D of the top part of the as-grown NWs (Figure 4b).

To elucidate the effect of the NW diameter on the absorptance without strong effects of the reflection losses, we turn to study the transmittance of the samples (Figure 4c). We find that the transmittance decreases monotonously with NW diameter and the agreement between modeling and experiments is excellent. Thus, since $A = 1 - R - T$, the peak found in the modeled absorptance at $D \approx$ 200 nm (Figure 4a) shows up due to the increasing reflection losses in the modeling with increasing D (Figure 4b). Therefore, our results demonstrate that by reducing the insertion reflection losses, the range of NW diameters suitable for absorption applications can be extended considerably. Our experimental results (Figure 4c) show that D > 200 nm is very suitable for high absorptance since the transmittance is less than

[b] We note that for L < 1000 nm the modeled reflectance can show higher values than 5 % and there are noticeable oscillations in the reflectance. These occur in these short NWs due to additional contribution from reflection from the NW/PDMS-PDMS bottom interface, located a distance L down from the top air-NW/PDMS interface (Figure 1b) .

Address correspondence to Nicklas Anttu, nicklas.anttu@ftf.lth.se

4 %. This low transmittance gives the prospect of A_{mean} > 96 %, provided that a suitable geometry is used for the NW part closest to the top interface to reduce the insertion reflection losses.

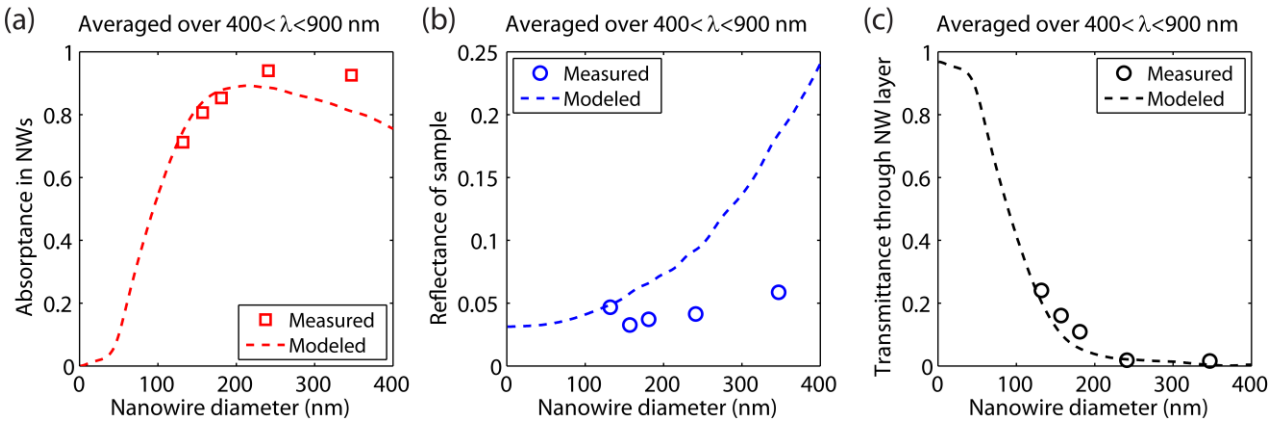

Figure 4. Measured and modeled wavelength-averaged absorptance, reflectance, and transmittance of NW arrays as a function of NW diameter *D*. The average length of the NWs on the fabricated samples lies in the range of L = 1441 ± 70 nm to 1663 ± 86 nm. The modeled NW arrays have NWs of length L = 1570 nm, which is the mean of the average lengths of the fabricated samples.

4. Conclusions

In conclusion, we have studied experimentally the absorption of light in InP NW arrays. The NWs were peeled off from the opaque growth substrate into transparent PDMS matrices to allow for determination of the absorption in the NWs without contribution from the substrate. Our measurements demonstrate that the NWs can absorb all the incident light with energy above the band gap energy which is coupled into the array, even if the NWs fill only a fraction of the volume of the NW array. Thus, also light that would travel between the NWs in a ray-optics description can interact efficiently with the NWs. We found that 2000 nm long NWs can absorb 94 % of the incident light. Furthermore, we identified the insertion reflection loss into the NW array as a very important parameter affecting the absorption of light. By reducing this reflection loss, the absorptance of a NW array does not show a clear optimum when it comes to the NW diameter. Instead, the absorptance increases monotonously with increasing diameter of the NWs.

Acknowledgments

This work was supported by the Swedish Research Council (VR), the Swedish Foundation for Strategic Research (SSF), the Swedish Energy Agency, the Nanometer Structure Consortium at Lund University (nmC@LU), the Nordic Innovation program NANORDSUN, and the Knut and Alice Wallenberg Foundation.

References

[1] Wallentin, J.; Anttu, N.; Asoli, D.; Huffman, M.; Åberg, I.; Magnusson, M. H.; Siefer, G.; Fuss-Kailuweit, P.; Dimroth, F.; Witzigmann, B.; Xu, H. Q.; Samuelson, L.; Deppert, K.; Borgström, M. T. InP Nanowire Array Solar Cells Achieving 13.8% Efficiency by Exceeding the Ray Optics Limit. *Science* **2013**, *339*, 1057-1060.

[2] Mariani, G.; Wong, P.-S.; Katzenmeyer, A. M.; Léonard, F.; Shapiro, J.; Huffaker, D. L. Patterned radial GaAs nanopillar solar cells. *Nano Lett.* **2011**, *11*, 2490-2494.

[3] Goto, H.; Nosaki, K.; Tomioka, K.; Hara, S.; Hiruma, K.; Motohisa, J.; Fukui, T. Growth of core-shell InP nanowires for photovoltaic application by selective-area metal organic vapor phase epitaxy. *Applied Physics Express*, *2*, 035004.

Address correspondence to Nicklas Anttu, nicklas.anttu@ftf.lth.se

[4] Cui, Y.; Wang, J.; Plissard, S. R.; Cavalli, A.; Vu, T. T. T.; van Veldhoven, R. P. J.; Gao, L.; Trainor, M.; Verheijen, M. A.; Haverkort, J. E. M.; Bakkers, E. P. A. M. Efficiency Enhancement of InP Nanowire Solar Cells by Surface Cleaning. *Nano Letters* **2013**,

[5] Vj, L.; Oh, J.; Nayak, A. P.; Katzenmeyer, A. M.; Gilchrist, K. H.; Grego, S.; Kobayashi, N. P.; Wang, S. Y.; Talin, A. A.; Dhar, N. K.; Islam, M. S. A perspective on nanowire photodetectors: current status, future challenges, and opportunities. *IEEE Journal of Selected Topics in Quantum Electronics* **2011**, *17*, 1002-1032.

[6] Svensson, J.; Anttu, N.; Vainorius, N.; Borg, B. M.; Wernersson, L.-E. Diameter-Dependent Photocurrent in InAsSb Nanowire Infrared Photodetectors. *Nano Letters* **2013**, *13*, 1380-1385.

[7] Kästner, G.; Gösele, U. Stress and dislocations at cross-sectional heterojunctions in a cylindrical nanowire. *Philosophical Magazine* **2004**, *84*, 3803-3824.

[8] Gudiksen, M. S.; Lauhon, L. J.; Wang, J.; Smith, D. C.; Lieber, C. M. Growth of nanowire superlattice structures for nanoscale photonics and electronics. *Nature* **2002**, *415*, 617-620.

[9] Björk, M. T.; Ohlsson, B. J.; Sass, T.; Persson, A. I.; Thelander, C.; Magnusson, M. H.; Deppert, K.; Wallenberg, L. R.; Samuelson, L. One-dimensional Steeplechase for Electrons Realized. *Nano Lett.* **2002**, *2*, 87-89.

[10] Wu, Y.; Fan, R.; Yang, P. Block-by-Block Growth of Single-Crystalline Si/SiGe Superlattice Nanowires. *Nano Lett.* **2002**, *2*, 83-86.

[11] Mårtensson, T.; Svensson, C. P. T.; Wacaser, B. A.; Larsson, M. W.; Seifert, W.; Deppert, K.; Gustafsson, A.; Wallenberg, L. R.; Samuelson, L. Epitaxial III−V Nanowires on Silicon. *Nano Lett.* **2004**, *4*, 1987-1990.

[12] Muskens, O. L.; Rivas, J. G.; Algra, R. E.; Bakkers, E. P. A. M.; Lagendijk, A. Design of Light Scattering in Nanowire Materials for Photovoltaic Applications. *Nano Letters* **2008**, *8*, 2638-2642.

[13] Hu, L.; Chen, G. Analysis of optical absorption in silicon nanowire arrays for photovoltaic applications. *Nano Letters* **2007**, *7*, 3249-3252.

[14] Hu, S.; Chi, C.-Y.; Fountaine, K. T.; Yao, M.; Atwater, H. A.; Dapkus, P. D.; Lewis, N. S.; Zhou, C. Optical, electrical, and solar energy-conversion properties of gallium arsenide nanowire-array photoanodes. *Energy Environ. Sci.* **2013**, *6*, 1879-1890.

[15] Anttu, N. Geometrical optics, electrostatics, and nanophotonic resonances in absorbing nanowire arrays. *Opt. Lett.* **2013**, *38*, 730-732.

[16] Anttu, N.; Xu, H. Q. Coupling of Light into Nanowire Arrays and Subsequent Absorption. *Journal of Nanoscience and Nanotechnology* **2010**, *10*, 7183-7187.

[17] Anttu, N.; Xu, H. Q. Efficient light management in vertical nanowire arrays for photovoltaics. *Opt. Express* **2013**, *21*, A558-A575.

[18] Kupec, J.; Stoop, R. L.; Witzigmann, B. Light absorption and emission in nanowire array solar cells. *Optics Express* **2010**, *18*, 27589-27605.

[19] Huang, N.; Lin, C.; Povinelli, M. L. Broadband absorption of semiconductor nanowire arrays for photovoltaic applications. *Journal of Optics* **2012**, *14*, 024004.

[20] Lin, C.; Povinelli, M. L. Optical absorption enhancement in silicon nanowire arrays with a large lattice constant for photovoltaic applications. *Optics Express* **2009**, *17*, 19371-19381.

[21] Anttu, N.; Xu, H. Q. Scattering matrix method for optical excitation of surface plasmons in metal films with periodic arrays of subwavelength holes. *Physical Review B* **2011**,

Address correspondence to Nicklas Anttu, nicklas.anttu@ftf.lth.se

83, 165431.

[22] Glembocki, O. J.; Piller, H. (1985) Indium phosphide (InP). *Handbook of Optical Constants of Solids*, ed E.D. Palik (Academic, Place) Ch. 503-516.

[23] Seo, K.; Wober, M.; Steinvurzel, P.; Schonbrun, E.; Dan, Y.; Ellenbogen, T.; Crozier, K. B. Multicolored vertical silicon nanowires. *Nano Letters* **2011**, *11*, 1851-1856.

[24] Wang, B.; Leu, P. W. Tunable and selective resonant absorption in vertical nanowires. *Optics Letters* **2012**, *37*, 3756-3758.

[25] Chattopadhyay, S.; Huang, Y. F.; Jen, Y. J.; Ganguly, A.; Chen, K. H.; Chen, L. C. Anti-reflecting and photonic nanostructures. *Materials Science and Engineering: R: Reports* **2010**, *69*, 1-35.

[26] Diedenhofen, S. L.; Janssen, O. T. A.; Grzela, G.; Bakkers, E. P. A. M.; Gómez Rivas, J. Strong geometrical dependence of the absorption of light in arrays of semiconductor nanowires. *ACS Nano* **2011**, *5*, 2316-2323.

[27] Fan, Z.; Kapadia, R.; Leu, P. W.; Zhang, X.; Chueh, Y.-L.; Takei, K.; Yu, K.; Jamshidi, A.; Rathore, A. A.; Ruebusch, D. J.; Wu, M.; Javey, A. Ordered Arrays of Dual-Diameter Nanopillars for Maximized Optical Absorption. *Nano Letters* **2010**, *10*, 3823-3827.

Address correspondence to Nicklas Anttu, nicklas.anttu@ftf.lth.se

Address correspondence to Nicklas Anttu, nicklas.anttu@ftf.lth.se